Tabletop Soft X-Ray Ptychography in Transmission Geometry

THESIS

submitted in partial fulfillment of the
requirements for the degree of

MASTER OF SCIENCE

in

APPLIED PHYSICS

Author : Joop Hendriks
Student ID : s2166968
Supervisor : Ra'anan I. Tobey
2nd corrector : Maxim S. Pchenitchnikov
Supervisor LANL : Richard L. Sandberg

Groningen, The Netherlands, March 31, 2017

Tabletop Soft X-Ray Ptychography in Transmission Geometry

Joop Hendriks

March 31, 2017

Abstract

Microscopes have proven to be an important tool in science. X-ray microscopes can reach higher resolution than regular optical microscopes because of the shorter wavelength, but due to the stronger interaction with matter no regular optics can be used. CDI and Ptychography are two methods that are used in this report to reconstruct a magnified image from the object from its diffraction patterns. These methods are a way to cope with the phase problem, as only amplitudes can be detected where information about the phase and amplitude is needed to make a reconstruction. Both methods were used in combination with tabletop measurements in a transmission geometry. For the measurement with CDI a laser in the visible range was used (633 nm) and the object reconstruction clearly showed the sample with all its features with a resolution of $3\mu m$. Soft x-rays with a wavelength of 29 nm were used for the ptychography measurements, generated by high harmonic generation. Several measurements have been performed with different parameters in an effort to get the first ptychographic reconstructions from this setup. The results are a reconstruction of the whole test object with a resolution of $3\mu m$ or $2\mu m$ if it is partly scanned.

# Contents

Chapter 1

Introduction

For hundreds of years, microscopes have helped researchers in many areas of science to look at nature in greater detail. Many discoveries could not have been made without the invention of the microscope. The well-known optical microscope uses a set of lenses and visible light to get a magnified image, but its resolution is limited by the relatively long wavelength of the visible light. The need for higher resolution resulted in the development of improved methods and other kinds of microscopy. Over the years, several Nobel prizes have been awarded for microscopy related research: the phase contrast microscope in 1953 [1, 2], work on electron microscope optics [3], the invention of the scanning tunneling microscope [4] in 1986 and most recently in 2014 for the development of super-resolved fluorescence microscopy [5, 6, 7]. In the search to higher resolution, scientists either had to reduce the wavelength or come up with clever tricks in order to 'beat the diffraction limit.'

In conventional microscopy, the Rayleigh criterion describes the minimal distance between two points at which they can still be resolved, δ [8],

$$\delta = \frac{0.61\lambda}{NA} = \frac{0.61\lambda}{nsin\theta} \qquad (1.1)$$

where $NA = nsin\theta$ is the numerical aperture of the optical system, θ is the half angle of the light incident on the object lens and n is the index of

1

refraction. This criterion can be graphically represented by the maximum of an Airy disk pattern that is generated by the diffraction of one point source, spatially coincides with the minimum of the Airy pattern an other point, as is shown in Fig. 1.1.
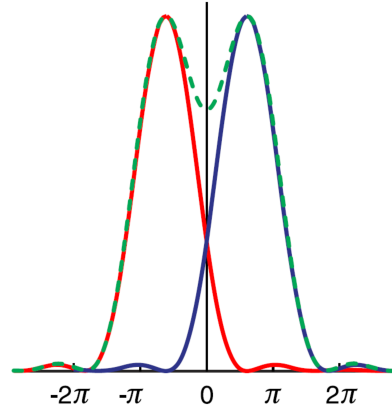
Figure 1.1: *The Rayleigh criterion for a circular aperture. The minimum distance at which two points are resolvable is when the maximum of the Airy pattern origination from one point is at the zero of the other [9]*

Looking at Eq. 1.1, the obvious options for increasing the resolution are decreasing the illuminating wavelength and/or increasing the numerical aperture. If visible light is the only option, one can increase the numerical aperture by decreasing the distance between lens and object, but this requires high quality lenses with short focal lengths.

Beside optical microscopes there are electron microscopes of different types, such as the transmission electron microscope (TEM) and the scanning tunneling electron microscope (STM). They make use of the very short de Broglie wavelength of electrons and can reach sub-Ångström resolutions of 0.05 nm [10]. However, electrons have several drawbacks compared to optical microscopes as they can only operate under ultra high vacuum due to the electron's strong interaction with matter, like the gas molecules in the beampath. This also makes it impossible to scan through thick samples as the mean free path of electrons is too short to propagate

through, for example, a cell. For this reason samples have to be heavily modified before they can be put under an electron microscope [11].

X-ray microscopy is somewhere in between optical microscopes in the visible range and electron microscopes. The soft x-rays that are used in this thesis have a shorter wavelength than visible light, which is good for the resolution. But contrary to visible light, soft x-rays do interact with matter, albeit less than electrons. This poses both challenges and opportunities for this field of microscopy. Like electron microscopes, the x-rays have to go through vacuum although the vacuum that is required is not as extreme. For the same reason it is also possible to look at thicker samples such as cells or even thin sheets of metals [12, 13]. However, due to this stronger interaction, it is no longer possible to use conventional refractive optics as they are opaque to the x-rays. Therefore alternative methods are needed to produce a magnified image of the object.

In this thesis two different methods for microscopy without refractive optics are used to reconstruct magnified images from the diffraction pattern(s) of the sample, namely coherent diffraction imaging (CDI) and ptychography. These methods require a coherent light source, which is not a problem for light in the visible range, as lasers can be used.

For a long time, synchrotrons were the only source for bright and coherent soft x-rays. However, the development of high harmonic generation (HHG) opened the way for tabletop experiments. Although the brightness of HHG sources is lower than that of a synchrotron, one has much more time for experiments as it is no longer necessary to apply for limited beam time at a synchrotron. By the development of tabletop CDI and ptychography we hope that these methods become a useful tool for future research in a broad range of scientific fields.

Chapter 2

Theoretical Background

2.1 Diffraction

Both CDI and ptychography are based on reconstructing an object from its diffraction patterns. Therefore it is important to fully understand the relations between the incoming light and the resulting diffraction patterns as that is what is used in the reconstruction algorithms. This section will treat the theory that explains these relations, known as Fourier optics, roughly following the discussion from Peatross and Ware [9].

Christiaan Huygens was the first to describe light as waves, in a time when Newton's theory, where light is seen as particles, was the norm. In his work *Traité de la Lumière* from 1690, he presented the idea that every point that disturbs the incoming wavefront will act as a source for spherical secondary wavelets that will have the same speed and frequency as the incoming light in the same medium. The resulting outgoing wavefront is the envelope of these wavelets [14]. This idea, known as Huygens' principle, is quite rudimentary and did not have a mathematical basis for several years. After Young showed the wave-like nature of light with his famous two slit experiment, Augustin-Jean Fresnel developed a mathematical framework for Huygens' theory. Adding up all secondary spherical wavelets (i.e. of the form e^{ikR}/R) originating from point sources that

4

are spaced an infinitesimal distance from each other, results in the diffraction formula:

$$E(x,y,z) = -\frac{i}{\lambda} \iint_{aperture} E(x',y',0)\frac{e^{ikR}}{R}dx'dy' \tag{2.1}$$

where x' and y' are the coordinates in the aperture plane (where $z'=0$), and x, y and z are the coordinates that define the plane of the screen. As is illustrated by Fig. 2.1, R, the distance from the source, can be written as

$$R = \sqrt{(x-x')^2 + (y-y')^2 + z^2} \tag{2.2}$$
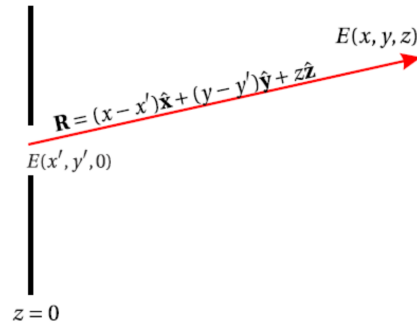
Figure 2.1: *Illustration of the parameters that are used in this chapter. [9]*

According to this equation light can as easily diffract in the reverse direction as in the forward direction, which is a consequence of Huygens' wavelet theory. This problem was solved by Kirchhoff by adding a factor known as the obliquity factor:

$$E(x,y,z) = -\frac{i}{\lambda} \iint_{aperture} E(x',y',0)\frac{e^{ikR}}{R}\left[\frac{1+cos(\mathbf{R},\hat{\mathbf{z}})}{2}\right] dx'dy' \tag{2.3}$$

where the cosine is of the angle between $(\mathbf{R}, \hat{\mathbf{z}})$.

Unfortunately, this equation is difficult to solve. By approximating the square root in eq. 2.2 with the first two terms of its binomial expansion (See Goodman for more details [8]), Eq. 2.3 can be rewritten to

$$E(x,y,z) \approx -\frac{ie^{ikz}e^{\frac{k}{2z}(x^2+y^2)}}{\lambda z} \iint\limits_{aperture} E(x',y',0)e^{i\frac{k}{2z}(x'^2+y'^2)}e^{-i\frac{k}{z}(xx'+yy')}dx'dy'$$

(2.4)

where $k = 2\pi/\lambda$. The exponential factors in front of the integral are global phase factors and do not change the measured intensity of $E(x,y,z)$. The left exponential in the integrand, representing the Fresnel phase, describes the propagation of the diffracted light in z, but is only relevant when z is small compared to the dimensions of the aperture. By omitting this factor from eq. 2.4, we arrive at a much friendlier looking Fraunhofer approximation:

$$E(x,y,z) \approx -\frac{ie^{ikz}e^{\frac{k}{2z}(x^2+y^2)}}{\lambda z} \iint\limits_{aperture} E(x',y',0)e^{-i\frac{k}{z}(xx'+yy')}dx'dy' \qquad (2.5)$$

which is valid if z is very large so that the screen is in the *far field*, or

$$z \gg \frac{k}{2}(x'^2 + y'^2) \text{ so that } e^{-\frac{ik}{2z}(x'^2+y'^2)} \approx 1 \qquad (2.6)$$

Physically this means that the diffraction pattern has evolved to its final form once it reaches the far field, where the diffraction pattern itself is just the two dimensional Fourier transform of the aperture. The Fraunhofer approximation is very relevant for most cases in this thesis, since all ptychography measurements were done in the far field.

2.2 CDI

In lensless microscopy, as the name already implies, there are no physical optics that perform the Fourier transform on the diffracted light to make a magnified image of the object. Instead, the light is captured by a detector, but it can only measure the intensity of the diffraction patterns and therefore the phase information of the pattern is lost. This loss is known as the phase problem, and it is the central problem of lensless microscopy.

Alternatively, phase retrieval algorithms are needed to find the information about the phase that is needed to get a real and magnified image of an object. One of these methods is CDI.

In 1952 Sayre stated in a short article that one can get enough information from intensity measurements, but only if it is sufficiently oversampled [15]. In that time, x-rays were already an important tool in crystallography and it could now be extended to noncrystalline materials or even biological tissue [16, 17]. At the basis of Sayre's idea is the Nyquist-Shannon sampling theorem, which states that certain functions can be reconstructed exactly from a limited number of samples. The frequency at which a sample of the function needs to be taken is known as the Nyquist frequency. For a function with a frequency not higher than B, the minimum sampling ratio must

$$\sigma = \frac{f_i}{B_i} \geq 2 \tag{2.7}$$

where f_i is the sampling frequency and $i = x, y, z$, depending on the number of dimensions. If the condition of Eq. 2.7 is not satisfied, the reconstructed function may exhibit *aliasing*: a function will be fitted in such a way that fits the sampling points but is not the original function. An illustration of aliasing is provided in Fig. 2.2.

Applying this to the detector in the image plane, this means that the diffraction pattern needs to be sampled at a frequency of least

$$f_i = \frac{D}{z\lambda}, \tag{2.8}$$

in both the x and y direction, where D is the sample diameter. Only when this is satisfied, e.g. when the object is sufficiently *oversampled*, a unique solution for the phase is guaranteed [19, 20]. As stated by Eq. 2.7, the ratio between the total pixel number (f_i) and the number of pixels with an unknown values (B_i), must be larger than two. Or in other words, one needs to know the values of at least half of the pixels. The solution to this is applying a *support* to the object: an opaque region that extends far enough so that it provides the necessary oversampling.
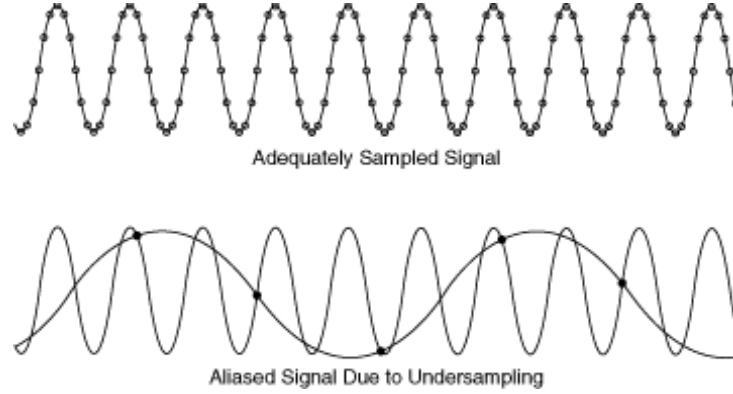
Figure 2.2: *With a sufficient sampling frequency, a periodic function can be reconstructed perfectly. If the sampling frequency is lower than the Nyquist frequency there is a risk of aliasing, where the reconstructed function has a lower frequency than the original function. [18]*

To quantify this statement, the derivation of the oversampling requirements will be treated, closely following the dissertation of Sandberg [21] and the paper by Miao and Chapman [16].

Most often, the diffraction patterns are measured by a CCD camera with $N \times N$ pixels. This implies that the object cannot be sampled at a higher rate than $N \times N$, so the number of pixels of the detector and the object is 'conserved'. Mathematically, a diffraction pattern in the far field is equal to the Fourier transform of the object, so

$$F(\mathbf{k}) = \mathcal{F}[f(\mathbf{x})] = \int_{-\infty}^{+\infty} f(\mathbf{x}) exp\left[2\pi i \mathbf{k} \cdot \mathbf{x}/N\right] d\mathbf{x}, \qquad (2.9)$$

where $f(\mathbf{x})$ is the density of the object. The Nyquist-Shannon sampling theorem allows to write Eq. 2.9 as

$$F(\mathbf{k}) = \sum_{x=0}^{N-1} f(\mathbf{x}) exp\left[2\pi i \mathbf{k} \cdot \mathbf{x}/N\right], \quad \mathbf{k} = 0, ..., N-1 \qquad (2.10)$$

provided that the sampling rate is at least equal to the Nyquist frequency. If $F(\mathbf{k})$ is sampled at twice the frequency so that

$$F(\mathbf{k}) = \sum_{x=0}^{N-1} f(\mathbf{x}) exp\left[2\pi i \mathbf{k} \cdot \mathbf{x}/(2N)\right], \quad \mathbf{k} = 0, ..., 2N-1 \qquad (2.11)$$

this again can be rewritten to:

$$F(\mathbf{k}) = \sum_{x=0}^{2N-1} g(\mathbf{x}) exp\left[2\pi i \mathbf{k} \cdot \mathbf{x}/(2N)\right], \quad \mathbf{k} = 0, ..., 2N-1, \qquad (2.12)$$

where $g(\mathbf{x})$ is a new function defined as:

$$g(\mathbf{x}) = \begin{cases} f(\mathbf{x}) & 0 \leq \mathbf{x} \leq N-1 \\ 0 & N \leq \mathbf{x} \leq 2N-1. \end{cases} \qquad (2.13)$$

What this means is that oversampling by twice the Nyquist frequency results in a region of double the size outside the object with zero density, known as the support. Fig. 2.3 gives an illustration of this. So vice versa, an opaque region on the outside of the sample, known as the *support* will increase the oversampling.

Often the sample size is known *à priori*, so it is important to know what happens in the detector plane to be able to fulfill the condition of Eq. 2.7. For a two dimensional array of pixels with size p, it is easy to see that the linear oversampling at the detector plane O is the square root of σ, where

$$O = \frac{1}{pf_D} = \frac{z\lambda}{Dp}, \qquad (2.14)$$

f_D the largest spatial frequency of the sample given by Eq. 2.8.

What remains is to derive the real size of the object under study. By using the conservation of pixels, the pixel size of the detector and the ones that are projected on the object can be related to each other, as is illustrated in Fig. 2.4. By noting that the oversampling ratio of Eq. 2.14 is equal to the L_{object}/N, where N is the number of pixels, we arrive at the expression

$$P_{object} = \frac{OD}{N} = \frac{Z\lambda D}{p_{det}ND} = \frac{z\lambda}{p_{det}N} \qquad (2.15)$$

which are all known quantities.
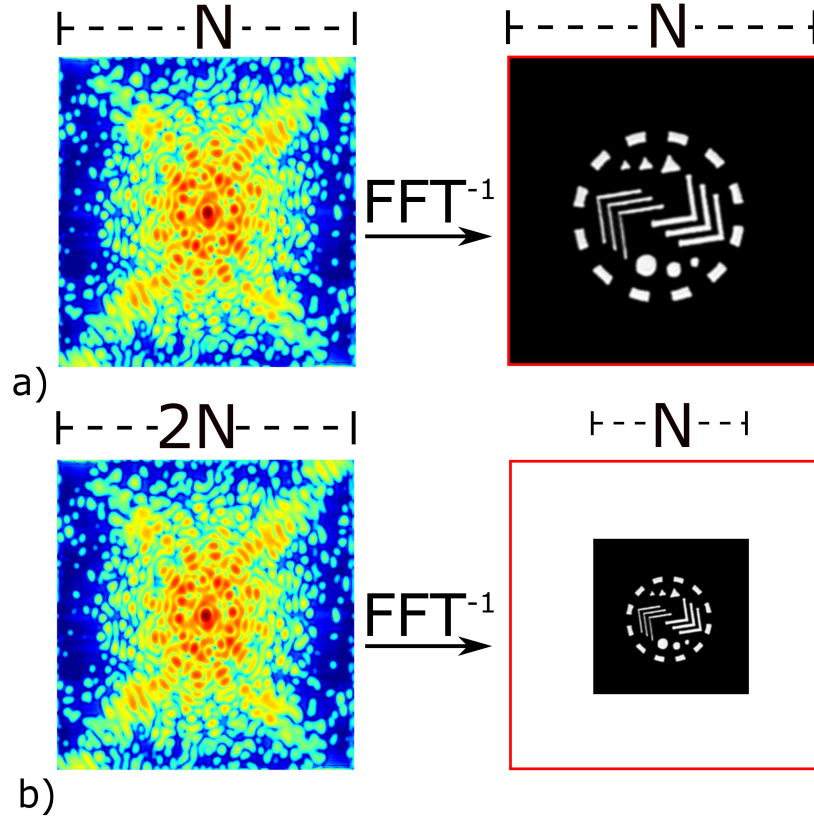
Figure 2.3: *An illustration of the support region that is generated when the object is oversampled. No light is scattered from this region. Image adapted from [21]*

2.2.1   Phase retrieval

While it was mathematically proven that the phase of the diffracted light can be reconstructed uniquely, it took twenty years before Gerchberg and Saxton published the first algorithms that could actually retrieve the phase [22, 23]. Not much later, the algorithm was generalized and improved by Fienup [24] and became known as the *Error-Reduction* (ER) algorithm because the error in this method decreases monotonically. The algorithm iterates back and forth between the object and Fourier domain by taking the discrete Fourier transform:

$$F(u) = \sum_{x=0}^{N-1} f(x) exp\left[-i2\pi iu \cdot x / N\right] \qquad (2.16)$$
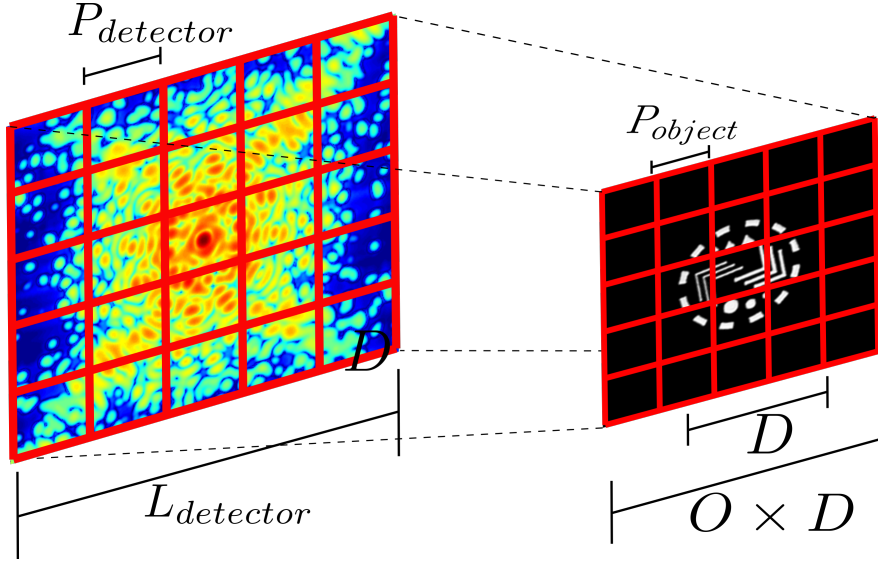
Figure 2.4: *Illustration of the relevant sizes in the detector and object plane. The number of pixels is conserved, which allows to convert $P_{detector}$ to P_{object}*

and its inverse:

$$f(x) = N^{-2} \sum_{x=0}^{N-1} F(u) exp\left[-i2\pi iu \cdot x/N,\right] \tag{2.17}$$

where $f(x)$ is a complex function

$$f(x) = |f(x)| exp\left[i\phi(x)\right] \tag{2.18}$$

The ER algorithm itself works at follows: once a measurement is done and a diffraction pattern is obtained, its amplitude, simply the square root of the measured intensity, is inserted into the algorithm as is shown in Fig. 2.5, in combination with a guess of the phase which is often 0 or random:

$$G'_k(u) = |F(u)| exp[i\phi_k(u)] \tag{2.19}$$

The inverse Fourier transform is than taken so that a first guess of the reconstruction is obtained:

$$g'_k(x) = |g'_k(x)| exp[i\theta'_k(x)| = \mathcal{F}^{-1}[G'_k(u)] \tag{2.20}$$
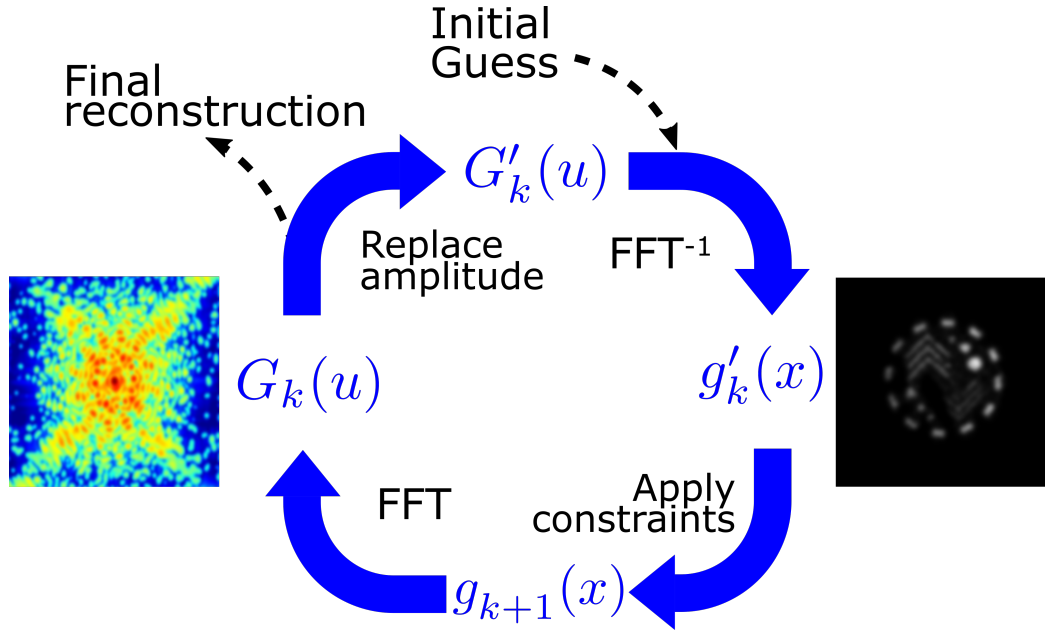
Figure 2.5: *An illustration of the iterative Fourier transforms of the ER algorithm showing the four stages of the ER loop and the operations that are performed between them.*

and the first guess of the reconstruction is then updated by the support constraint and the non-negativity constraint, which are there for purely physical reasons. The support is, contrary to before, now defined as the region in the current estimate of the object that contains the transparent parts, outside of which no light will be diffracted. Due to the requirement of oversampling, there is always a region that falls outside the support and if there are non-zero intensities in that region in the current guess, they have to be put to zero. Or formulated differently:

$$g_{k+1}(x) = \begin{cases} |g_k'(x)| & \text{if } x \text{ is inside the support region} \\ 0 & \text{if } x \text{ is outside the support} \end{cases} \tag{2.21}$$

The non-negativity constraint is there for the physical reason that the mod-

ulus of the complex value intensity cannot be negative, which means that

$$g_{k+1}(x) = \begin{cases} g_k'(x) & \text{if } Re(g_k'(x)) > 0 \\ 0 & \text{if } Re(g_k'(x)) < 0 \end{cases} \tag{2.22}$$

Taking the Fourier transform of this improved guess results the diffraction pattern of this guess, which is an approximation of the measured diffraction pattern, both in terms of phase and amplitude:

$$G_{k+1} = |G_{k+1}(u)|exp[i\phi_{k+1}(u)] = \mathcal{F}[g_{k+1}(x)] \tag{2.23}$$

The final step in this loop is to update the guess of the amplitude, and since this value is measured, the guess can be replaced by the real value:

$$G_{k+1}'(u) = |F(u)|exp[i\phi_{k+1}(u)] \tag{2.24}$$

This loop can be repeated until the value of $\sum_x |g_k'(x)|$ is closer to the real value $\sum_x f_k(x)$ than a specified error or until a maximum number of loops is reached. Although the error in the ER will reduce monotonically, it does not reduce very fast. An improved algorithm that converges much faster, despite being very similar to the ER algorithm, is known as the Hybrid Input-Output (HIO) algorithm [25]. The HIO algorithm approaches the phase problem slightly differently though. The first three steps, namely taking the Fourier transform $g(x)$, satisfying the Fourier constraints and taking the inverse Fourier transform again, are the same is in the ER algorithm. But in the case of the HIO algorithm, they are viewed as a single operation that can be thought of as a non-linear system with $g(x)$ as an input and $g'(x)$ as an output, where the output will always satisfy the Fourier constraint. In contrast to the ER algorithm, $g(x)$ no longer represents the best estimate of the reconstructed object, but rather a driving function for the next output [25]. With this in mind, the step that closes the loop from $g'(x)$ to $g(x)$ can be changed to

$$g_{k+1}(x) = \begin{cases} g_k'(x) & \text{if } x \text{ is inside the support region} \\ g_k(x) - \beta g_k'(x) & \text{if } x \text{ is outside the support} \end{cases} \tag{2.25}$$

where β is a constant that is normally around 0.7.

In the two methods described above, the support region is determined by computing the auto-correlation of the current best estimate of the object. However, a better estimate of the support will improve the rate of convergence toward a good reconstruction as the Fourier constraints will now be applied more accurately. The algorithm that was used in this report for that purpose is the Shrink-wrap algorithm [26, 27]. It too starts with the autocorrelation of the first guess of the object to get a first estimate of the support, but from then on the algorithm takes the convolution of $|g_k(x)|$ and a normalized Gaussian with a width σ, which is a specified number of pixels. So now, contrary to the autocorrelation, the estimate of the support can contain multiple peaks where the new support can be wrapped around, hence the name of the algorithm. The new support is then the region where the height convolution is larger than a certain threshold that can be changed to influence how tight the support is wrapped around the peaks. Finally, σ gets updated for the next iteration by decreasing it until after a number of iterations it reaches a specified minimum to prevent it from shrinking the support too much.

Distorted phase object

The reconstruction algorithms as mentioned above only work in the Fraunhofer regime, where the relation between the object and its diffraction patterns is a simple Fourier transformation without any additional phases. In section 2.1 it was mentioned that the the approximation for the Fraunhofer regime is only valid if $z \gg \frac{k}{2}\left(x'^2 + y'^2\right)$, or in other words, the Fresnel number F needs to be much smaller than 1, so that

$$F = \frac{a^2}{z\lambda} \ll 1 \tag{2.26}$$

where a is the characteristic size of the object. While it is clearly the easiest to do reconstructions in the Fraunhofer regime, there are certain benefits for moving to the Fresnel regime, where z is getting smaller and

Eq. 2.26 is no longer valid. This includes the ability to capture information from higher angles, as well as an improvement in reconstruction resolution and convergence speed [28]. Xiao and Shen proposed a universal solution that can be incorporated in the existing methods so that they can also be used for measurements in the near field. The key component of it is the introduction of a phase distorted object to Eq. 2.4, so that it becomes

$$E(x,y,z) \approx -\frac{ie^{ikz}e^{\frac{k}{2z}(x^2+y^2)}}{\lambda z} \iint\limits_{aperture} \overline{E}(x',y',0)e^{-i\frac{k}{z}(xx'+yy')}dx'dy' \quad (2.27)$$

where the distorted object is defined as

$$\overline{E}\left(x',y',0\right) \equiv E(x',y',0)e^{i\frac{k}{2z}\left(x'^2+y'^2\right)} \quad (2.28)$$

Thanks to this mathematical reinterpretation of Fresnel phase, it is possible again to evaluate the function by a Fourier transform, as it is for the Fraunhofer regime. The only difference is that the distorted object now represents the electric field at the object, but it is modified so that the Fresnel phase is included in it. Since the only difference between the original and the distorted object is this added phase, it is still possible to apply the real-space constraints (the measured amplitudes) to the distorted object, so that it can be implemented in the phase retrieval algorithms without any problems.

2.3   Ptychography

A different approach to the phase problem is ptychography. Contrary to CDI, samples do not have to be isolated for ptychography. It can be challenging to engineer such an isolated sample, and relaxing this requirement is a big benefit for biological and complex inorganic samples [29, 30, 31]. Instead of using a large beam that covers the sample, a much smaller beam is used to scan the object in a raster pattern by either moving the beam or

the sample position. As for CDI, it is also necessary in ptychography to have sufficient oversampling, but in the case of ptychography the oversampling is independent of the probe size [32]. Instead, it is the overlap of the area illuminated by the probe at neighbouring positions that determines the degree of oversampling. Let's consider a situation as illustrated in Fig. 2.6, where a square beam with size D illuminates the sample with steps of size R. In the case where $D = R$, the whole sample will eventually be illuminated but there is no overlap between the probe, as if each position is a separate experiment. In Fourier space, it means that the sample is illuminated by beam of size U, where $U = 1/D$, exactly the Nyquist sampling frequency. If the step size is decreased so that $D > R$, it will result in under-sampling in the detector plane because of the inverse relationship between it and the object plane. This is what is illustrated with the solid green line in Fig. 2.6. A consequence of this is that in the gray areas are corrupted by aliasing, because in Fourier space these areas are not sampled anymore. The parts that are outside the tile add to the opposite side as they wrap around the tile. To quantify this, the function $\alpha_U(\mathbf{r})$ is introduced, which is a measure of the non-uniqueness of the object estimate within a tile [32]. The ambiguity at coordinate $\mathbf{r}$ can be expressed as $\alpha_U(\mathbf{r}) = 1/n$, where n is the number of times the object has been superimposed on itself. The outcome of this function is depicted in the figure for the all three cases. At the same time, these areas are overlapped by adjacent illumination positions from the ptychography raster by an amount described by the function $\pi_R(\mathbf{r})$. Since $\pi_R(\mathbf{r})$ is the inverse of $\alpha_U(\mathbf{r})$, we can conclude that $\pi_R(\mathbf{r})\alpha_U(\mathbf{r}) = 1$, or in other words, the additional redundancy that is obtained from increasing the probe size compensates for the additional ambiguity. This is not only valid for a square probe, but for any arbitrary shape. However, if there are small deviations in the raster pattern, which is the usual practice in order to prevent the emergence of periodic artifacts in the reconstruction [33], this is no longer valid and the oversampling will drop. Fortunately this can be solved easily by decreas-

ing the step size so that the oversampling requirement is satisfied again for all points [32].
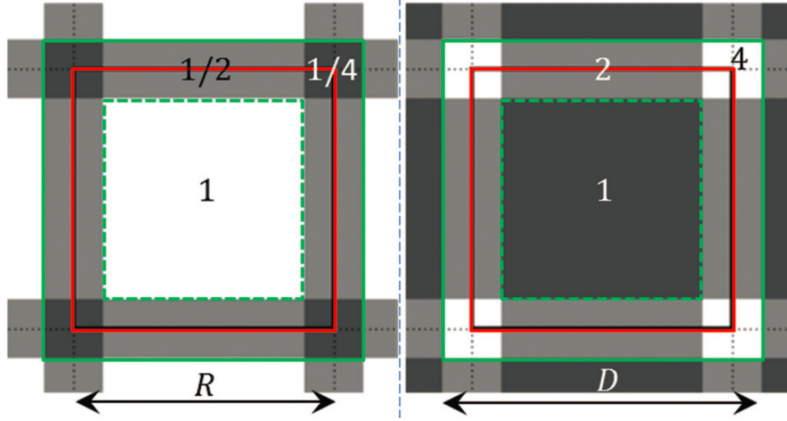
Figure 2.6: *An illustration of the conversion of information density in the object plane (left) and the detector plane (right), with the values of $\alpha_u(mathbfr)$ and $\pi_R(\mathbf{r})$ for the different cases displayed in respectively the left and right figure [32].*

2.3.1   Phase retrieval

One of the most popular, stable and efficient phase retrieval methods in ptychography is the extended Ptychographic Iterative Engine (ePIE) algorithm [34]. As the name already implies, it is an extension from the Ptychographic Iterative Engine (PIE) [35]. One of the larger differences between PIE and the methods described in Section 2.2.1 is that PIE also makes a reconstruction of the probe, in addition to the object.

PIE uses two complex functions, the object function $O(\mathbf{r})$ and the probe function $P(\mathbf{r})$, that can be moved relative to each other by a step size $\mathbf{R}$. The product of these two functions will give the *exit wave function*

$$\psi(\mathbf{r}, \mathbf{R}) = O(\mathbf{r})P(\mathbf{r} - \mathbf{R}), \qquad (2.29)$$

which is the view of the object illuminated by the probe. A major drawback is that the PIE algorithm needs an accurate estimate of the probe in-

tensity and phase, something that is difficult to achieve. The ePIE algorithm doesn't need this as it can solve for the object and the probe separately [34, 33].

Another major difference with respect to CDI is that it is important to accurately know the positions of the sample relative to the beam for each point of the raster. Because of the scanning over many points and the amount of overlap between each position, the ptychography generates more data, much of it being redundant. As ePIE makes use of all this information, it is a more robust method compared to CDI [36].

The algorithms starts with making initial guesses for the probe wavefront and the object. One can start from a random guess and let the algorithm do the rest, but more accurate guesses will result in faster convergence. If the size of the probe is known *à priori*, one can assume it is Gaussian and use the size to make a good approximation of it. Information about the object is generally unknown, and thus a random guess or a constant number must be used to make a guess, with either a random or a constant object phase estimate.

Similar to the CDI phase retrieval methods, ePIE also iterates back and forth between real space and Fourier space, see Fig. 2.7 for a flowchart of the algorithm. The initial guesses are then multiplied according to Eq. 2.29 to obtain the exit wave function. The Fourier transform of it is an estimate the far field diffraction pattern that is measured, so the measured intensities can be used to replace the guessed intensity. The updated exit wave $\psi'_j(\mathbf{r})$ is then calculated by taking the inverse Fourier transform of it. The last step of ePIE is to update the object and probe functions that can be fed into the next iteration. The object update function is

$$O_{j+1}(\mathbf{r}) = O_j(\mathbf{r}) + \alpha \frac{P_j^*(\mathbf{r} - \mathbf{R}_{\mathbf{s(j)}})}{|P_j(\mathbf{r} - \mathbf{R}_{\mathbf{s(j)}})|_{max}^2} \left(\psi'_j(\mathbf{r}) - \psi_j(\mathbf{r}) \right), \qquad (2.30)$$

where P_j^* is complex conjugate of the probe function, and α is a parameter that controls the step size of the update function. Similarly, the probe
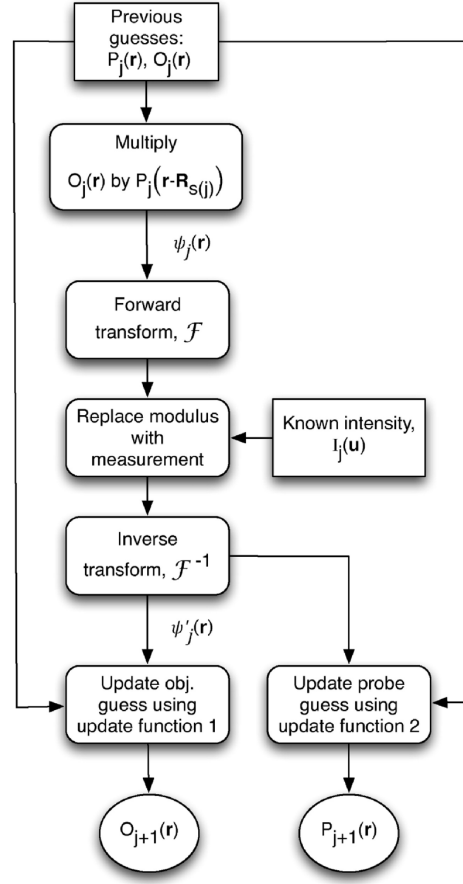
Figure 2.7: *A flowchart of the ePIE algorithm. An initial guess for the probe and the object is made and provided to the algorithm at $j = 0$ [34].*

update function is

$$P_{j+1}(\mathbf{r}) = P_j(\mathbf{r}) + \beta \frac{O_j^*(\mathbf{r} + \mathbf{R}_{\mathbf{s(j)}})}{|O_j(\mathbf{r} + \mathbf{R}_{\mathbf{s(j)}})|^2_{max}} \left(\psi_j'(\mathbf{r}) - \psi_j(\mathbf{r}) \right), \qquad (2.31)$$

where β has the same function as α. Both update functions divide out the current probe/object function from the corrected exit-wave, and then take the weighted average of this function and the current object/probe guess, where the weights are proportional to the current estimate [34]. This is done for all positions in a random sequence, and only after the object and probe functions for all positions are updated, a single ePIE iteration is completed.

2.4 High Harmonic Generation

Until the discovery of HHG [37], it was difficult if not impossible to generate coherent light with wavelengths below 100 nm with lasers. In that time, up-converting light was considered a perturbation process in non-linear optics. According to this theory, the intensity will drop by orders of magnitude for each step. However, in HHG, where the electric field of a high power laser interacts with atoms in a gas jet, one can observe a broad *comb* of odd harmonics that have roughly the same intensity up to a certain threshold, and it makes clear that treating HHG as a perturbation is no longer valid.

2.4.1 Three step model

The development of ultrafast lasers opened up the way for tabletop experiments, i.e. experiments that fit on one or two optical tables in a normal laboratory room. In the 1990's, lasers became powerful enough, while able to operate at femtosecond timescales at a large bandwidth [38]. Their ultrafast pulses are generated when the laser is *modelocked*. When a large number of frequencies are supported by the gain medium and the laser cavity, these modes will interfere and the result is an electric field that is zero most of the time, except for some very short pulses. After these short pulses leave the laser cavity, they can be amplified further to make them intense enough for producing high harmonics.

Since perturbation in non-linear optics can't describe HHG accurately, an intuitive theory known as the *three-step model* was developed [39]. When a strong laser field interacts with an atom, and its field strength approaches the Coulomb force that binds the outermost electrons of the gas atom, it can ionize it. Once the electron is liberated from the atom, the laser field accelerates it back to the parent ion where it can recombine. The excess energy (kinetic energy) is then released in the form of an x-ray photon, as is illustrated in Fig. 2.8.
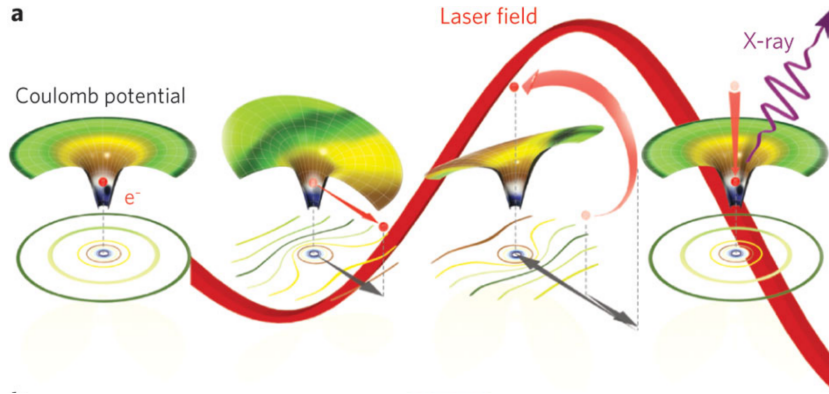
Figure 2.8: *Schematic of HHG. The first step ionizes an electron through tunnel ionization, after which it is accelerated back towards the nucleus of the same atom. A recollision event releases the excess energy as a high energy photon [40].*

The first step in this model is the ionization of atoms in the gas medium by the electric field of the laser. Depending on the field strength of the driving laser beam, this can occur in three different ways [38], illustrated by Fig. 2.9.
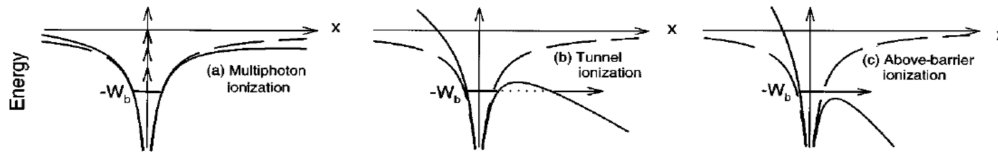
Figure 2.9: *The three regimes of atomic ionization. When an atom is exposed to a laser field that is weak compared to the Coulomb potential (dashed line), the effective potential (black line) is slightly affected and multiple photons are needed for ionization. As the laser intensity increases and approaches the strength of the Coulomb potential, the electron is allowed to tunnel through the reduced potential barrier. At even higher laser intensities the coulomb barrier is completely suppressed and the electron can travel freely [38].*

A common measure to determine which of the processes will occur is the Keldysh parameter, given by

$$\gamma = \frac{\omega \sqrt{2mI_p}}{eE} \tag{2.32}$$

where ω is the laser frequency, m and e are the electron mass and charge, respectively, I_p is the ionization potential of the valence electron and E magnitude of the peak electric field of the laser. For the limiting case where $\gamma \gg 1$, i.e. a weak field strength and/or a low frequency ω, multi-photon ionization is the mechanism that will occur. Several photons from the driving laser are absorbed and allow the electron to be ionized. The other limiting case, when $\gamma \ll 1$ is called barrier suppression. The potential of the atom tilts until one side is lower than the potential of the valence electron, which makes it ionized.

In HHG, it is the regime that is in between these two limiting cases, the *tunneling ionization*, that is relevant. In this regime, the laser intensity is high enough to distort the barrier such that only a narrow barrier prevents the electron from ionization [38]. After ionization the second step takes place: the electron acceleration. The laser field is much larger than the coulomb potential once the electron is ionized, which can be neglected at this point. The movement of the electron is classically described by [39]:

$$x = x_0 cos\omega t + v_0 t + x_0 \tag{2.33}$$

and

$$v_x = v_0 sin\omega t + v_0 \tag{2.34}$$

where ω is the laser frequency, x_0 is the initial displacement of the electron from the ion and v_0 is the initial velocity after tunneling. The velocity at which the electron will hit the parent ion is determined by the initial phase with respect to the driving field of the oscillating portions in Eq. 2.33 and 2.34, which is zero when the electron tunnels at the peak of the field. Once the direction of the driving field changes according to the same equations, the electron is accelerated towards the parent ion. The highest velocity is obtained when the initial phase equals 17.2 $^\circ$.

The kinetic energy is, in addition to the ionisation potential, emitted upon recombination with the parent ion as a high harmonic photon. The result of this is the emission of harmonics that form an intensity plateau with a maximum energy of

$$E_{max} = I_p + 3.2U_p \tag{2.35}$$

where I_p is the ionization potential of the atom, and U_p is the pondero-motive energy of the atom, the average kinetic energy in a sinusoidal field, given by

$$U_p = \frac{e^2 E^2}{am\omega^2} \propto I\lambda^2 \tag{2.36}$$

where e and m are the electron charge and mass and E, ω, I and λ are the energy, frequency, intensity and wavelength of the incident light [41]. From this, we can conclude that the longer wavelengths and higher intensities will result in higher cut-off energies. Interesting to note is that only odd harmonics are formed. The reason behind it is that the harmonics are produced by a series of bursts in a short time which are separated by half the laser period, these are the moments when the electrons and the atom recombine. In the Fourier transformed frequency space, it means that it forms a comb of harmonics separated by twice the frequency of the driving laser. Together with the fact that gas must have inversion symmetry, the induced polarization of the gas must be an odd function of the electric field, resulting in a comb of only odd harmonics [42].

2.4.2 Phasematching

One important requirement for HHG is that the phase velocity of the incident laser light v_l and that of the emitted x-rays v_{x-ray} are ideally matched so that only constructive interference occurs between photons generated at different spatial regions along the propagation path.

Fig. 2.10 a) and b) illustrate what happens when the HHG process is not properly phase matched. The high-harmonic signal can only increase when the difference in relative phase difference between the driving laser light and the high-harmonics is less than π radians. For a harmonic of order n, the coherence length is $l_c(n) = \pi/\Delta k_n$, where Δk_n is the phase mis-
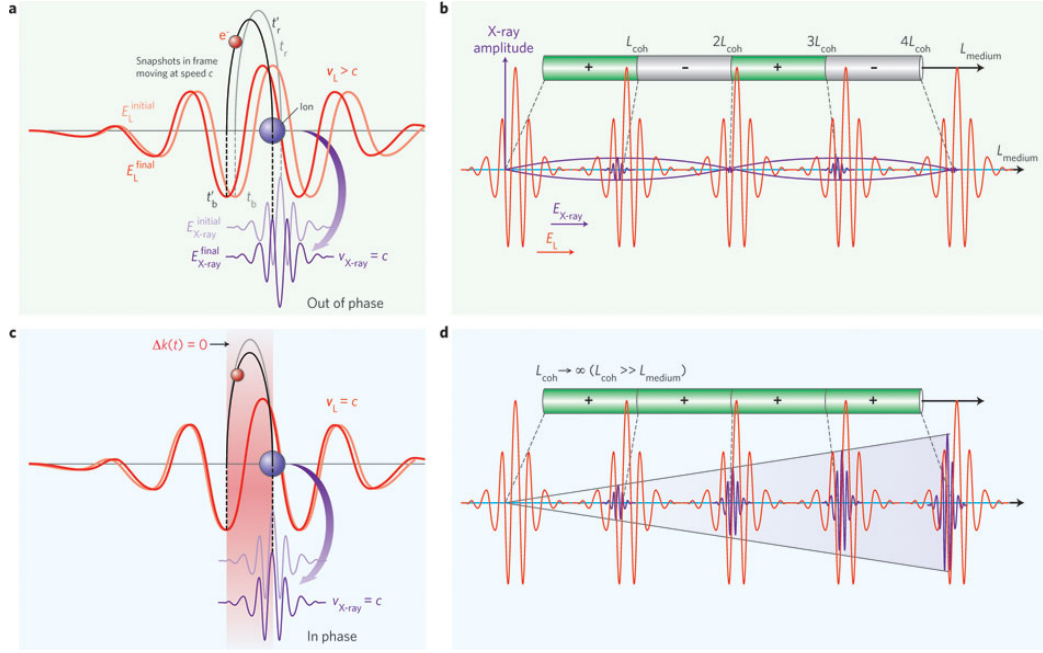
Figure 2.10: *Figure a) and b) show non-phase-matched build-up, showing alternating constructive and destructive interference of the x-rays with a period equal to coherence length, preventing a strong HHG signal build-up. The laser and HHG are plotted at the input ($E_l^{initial}$ and $E_{x-ray}^{initial}$) and output (E_l^{final} and E_{x-ray}^{final}) of the medium. c) and d) shows the same but now phase matched, where the signal increases linearly with distance [40].*

match between the two, and only within this length can coherent build-up take place [40]. The phase difference, together with the fact that the gas medium is often not transparent and is ionized while the harmonics are generated, result in a temporally and spatially changing index of refraction. The result is that the high-harmonics are periodically constructively and destructively added, as is illustrated in Fig. 2.10. Another factor in the phase matching in a gas jet, which is the case in this report, is the Gouy phase. When a Gaussian beam is focused, the phase will change by π on either side of the beam waist. Both the Gouy and the dipole phase of the beam, which depends on the distance from the focus position, need to be tuned in order to get a high intensity beam [43]. By focusing the beam

in front or behind the gas jet, it is possible to balance between the Gouy phase shift and the laser field strength. This is illustrated by Fig. 2.11
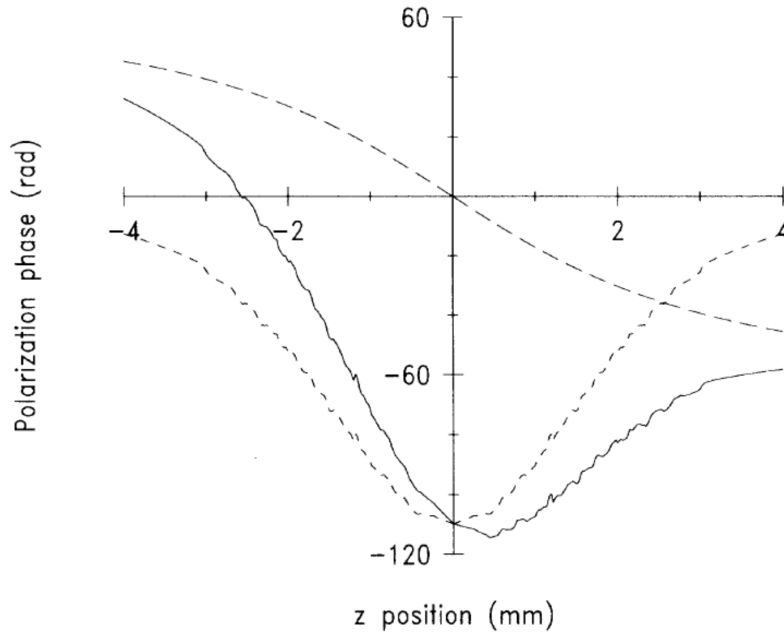

Figure 2.11: *The phase of the driving laser on the propagation axis (solid line). It is the addition of the Gouy phase (dashed line) and the bipolar phase (dotted line). By changing the position of the focus (and thus the zero of the Gouy phase) one can tune the phase in the jet [43].*

2.5   Coherence

One very important requisite for the reconstruction algorithms is that the light illuminating the sample is sufficiently coherent, or in other words, the phase relationship of the light must be well defined in either space or time. In this section the theory of coherence for short wavelengths will be covered in more detail, and why light generated by HHG is suitable to use in CDI and ptychography.

Since light can be described as a wave propagating in space, the coher-

ence of this wave needs to specified in two directions across this electro-magnetic wave [44]. Spatial coherence is related to the size of the source and the angular spread of the beam, and is the property of an electromagnetic wave to have a well defined phase at two points that are separated in a direction perpendicular to the direction of propagation. Temporal coherence, on the other hand, is a measure of how monochomatic the beam is, and indicates how correlated fields offset by time are. Fig. 2.12 illustrates the two types of coherence.

$$\xi_t = z\Delta\theta$$
$$= \frac{z\lambda}{2\pi d}$$

$$\xi_l = \frac{\lambda^2}{\Delta\lambda}$$
$$= c\tau_c$$
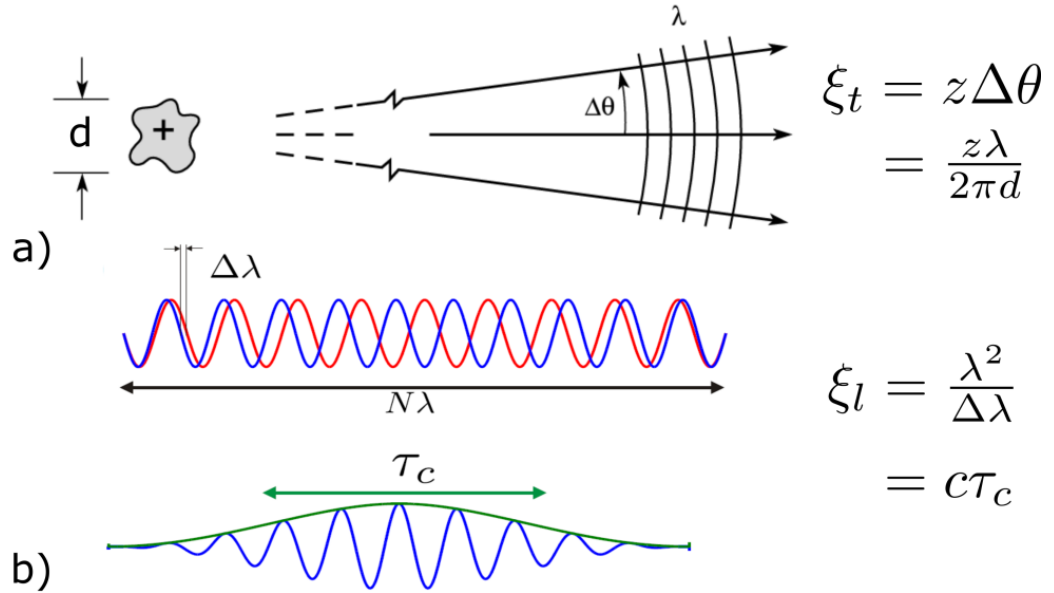
Figure 2.12: *An illustration of spatial and temporal coherence. a) shows how the temporal coherence length ξ_t depends on the distance along the propagation axis and the diversion angle θ [44]. b) shows how the longitudinal coherence length depends on the bandwidth $\Delta\lambda$ [9].*

To achieve perfect spatial coherence, one would need a plane wave that has the same phase on all points transverse to the direction of propagation. But since it is not possible to generate such a wave, the best one can do is to generate a spherical wave originating from a point source as it will approach a plane wave far from the source. But also the point source is not an realistic assumption, and in real life a source will always have some fi-

nite size. Increasing the source size from a point source, the emitted wave-fronts will get less spherical due to the uncorrelated radiation coming from the individual radiators, i.e. atoms, electrons etc., reducing the coherence of the wave [21]. The dependency of the spatial coherence of these parameters can be derived from Heisenberg's uncertainty relation[44]:

$$\xi_t = z\Delta\theta = \frac{z\lambda}{2\pi d} \tag{2.37}$$

where $\Delta\theta$ is the divergence angle (see Fig. 2.12) and d is the source diameter.

One can also derive a measure of temporal coherence. Contrary to spatial coherence, which is a measure of beam quality of a source, temporal coherence can also be viewed as a measure of the temporal bandwidth of the source. Therefore, the temporal coherence can be quantified by the longitudinal coherence length, given by [44]

$$\xi_l = \frac{\lambda^2}{\Delta\lambda} \tag{2.38}$$

Which can be interpreted as the number of wavelengths for which a wave has strong longitudinal coherence.

2.5.1 Gaussian modes

HHG generates a Gaussian beam, and therefore it is important to know what the coherence properties of such a beam is. The transverse coherence is equal to the divergence of the beam in the far field. This can be derived by the following: the radius at which the intensity is $1/\sqrt{e}$ of a Gaussian beam, as shown in Fig. 2.13, can be described mathematically by

$$r(z) = r_0\sqrt{1 + \left(\frac{\lambda z}{4\pi r_0^2}\right)^2} \tag{2.39}$$

where z is the distance from the source and r_0 is the beam waist, the smallest radius [44]. So in the far field where $z \gg 4\pi r_0^2/\lambda$, the divergence angle

θ can be calculated:

$$\theta = \frac{r(z)}{z} = \frac{\lambda}{4\pi r_0} \qquad (2.40)$$
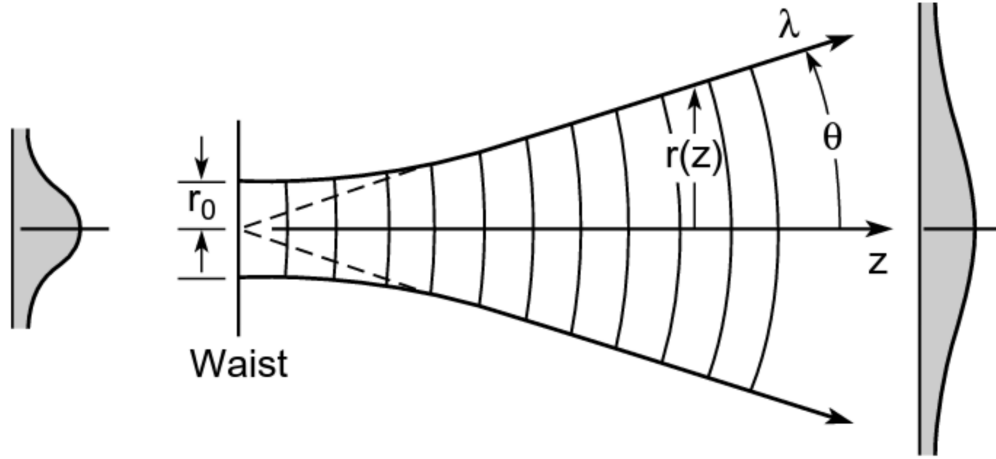
Figure 2.13: *[44]*

When this is rewritten for the beam diameter $d = 2r_0$, we get

$$d \cdot \theta = \frac{\lambda}{2\pi} \qquad (2.41)$$

which is the same as Eq. 2.37. So, in other words, a Gaussian beam exhibits perfect spatial coherence. This conclusion is supported by measurements of beams generated by HHG, which show high degrees of spatial coherence. [45]. The produced beam is a coherent Gaussian beam, since the driving laser is coherent and Gaussian too, as was explained in section 2.4. The phase matching is crucial in this case. If not done properly, the strongly varying index of refraction of the ionized gas will prevent coherent buildup of the flux and destroys the mode quality of the harmonic generation process [45]. If, however, the phase is matched, one can expect a spatial coherence length of several times the wavelength, so HHG is mostly limited by its temporal coherence [21].

3

Experimental methods

3.1 CDI

To collect the CDI data, a setup as shown in Fig. 3.1 was used.
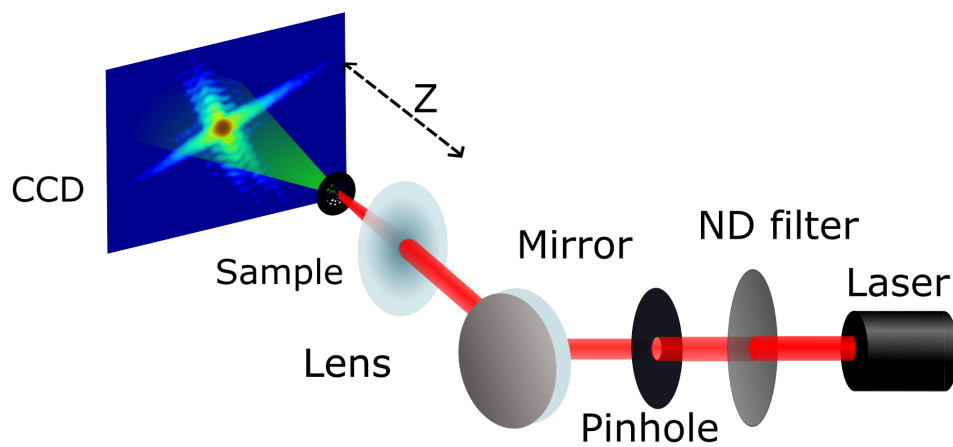
Figure 3.1: *Experimental setup for CDI. The laser beam enters the setup after which it is attenuated by an ND filter. It then goes through a pinhole so that only the central part of the beam is transmitted, after which the beam is directed towards a lens, focusing the beam on the sample. A detector measures the intensity of the resulting diffraction pattern.*

A Helium-Neon (HeNe) laser was used as a source of the coherent light

29

with $\lambda = 633$ nm. After that, the beam passes through a neutral density filter wheel that variably attenuates the laser beam intensity. A pinhole then selects the central portion of the beam and provides for a Gaussian illumination of the sample, so that a clear diffraction pattern can be generated. A lens with a focal length of 10 cm focuses the beam on the sample, illuminating it with a size (e^{-2}) of 90 μm. The sample itself is a pattern (see Fig. 3.2) with a diameter of 150μm machined in a thin stainless steel disk. It was centered so that the zeroth order beam was caught on the center of the detector.
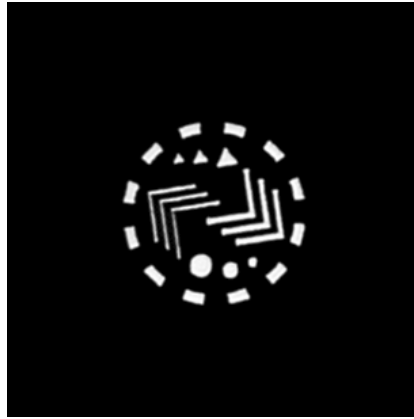
Figure 3.2: *The sample that was used for CDI and ptychography. It consists of a metal disk with transparent rectangles, triangles, circles and chevrons of different dimensions.*

The detector, a 1024 x 1280 pixel camera with a pixel size of 5μm, was placed on a slider on a rail so the sample to detector distance could be changed easily.

For a high resolution one wants to measure at a large numerical aperture, but the dynamical range of the camera will limit the maximum angle at which light can be captured. The intensity at the edges of the detector will be of several orders of magnitude less than at the center, more than the dynamical range can cope with. This problem is solved by collecting the diffraction patterns at two different exposure times. One is short enough so that the camera does not saturate at the brightest areas of the diffrac-

tion pattern, similar to a regular measurement. Care needs to be taken to make sure that the detector still operates in the linear regime for all the pixels, as CCD cameras deviate from a linear intensity to pixel value relation close to the saturation value. The other exposure time needs to be long enough to detect light at the detector edges while the camera will be saturated in the center. These two images are then stitched together in a MATLAB code to increase the dynamical range of the detector artificially, resulting in an image of the diffraction pattern where features at both the center and the edges are clearly visible. The code searches for pixels with a value higher than a preset threshold, mostly 65 % of the intensity of the saturated points, to ensure that the camera is in its linear regime for all the pixels that fall below this threshold. All points where the value exceeds the threshold will be deleted. The short exposure time data will then be scaled so that it connects smoothly to the high exposure image. The final step before the images are used to make a reconstruction is to smoothen high frequency noise that is present in the stiched image by applying a Gaussian filter to it.

3.1.1 Reconstruction

After these steps are done, the image of the diffraction pattern can be used to make a reconstruction. It is possible to use either the ER or the HIO algorithm as discussed in section 2.2.1, but combinations of algorithms can be faster and more efficient with better results. For example, the HIO algorithm is often used in combination with the ER algorithm as a few ER iterations after some more HIO iterations will decrease the estimated error quickly. In the method used in this experiment, both the HIO and the ER algorithms were used, as well as the shrink wrap algorithm. The big benefit of also including a few iterations of the shrink-wrap method is that it increases the quality of the guess of the support, as it is wrapped much tighter much faster around the reconstructed object than with the HIO+ER alone. The error-estimate that was used is the error between the

current intensity guess and the measured intensity values, or

$$E = \sqrt{|\sum \mathcal{F}(g) - F|} \tag{3.1}$$

The code will stop reconstructing once the error is below a pre-set threshold, or exceeds the maximum number of iterations, which is more often the case.

3.2 Ptychography

Ptychography is in theory a more robust method than ordinary CDI, but a big part of the advantage over visible light CDI is counterbalanced by the lower beam quality in x-ray ptychography [46]. Most effort was put into getting a beam of a high enough quality to be able to reconstruct the object. The setup that was used consists of two parts: in the first part an intense femtosecond pulse is generated, which is then directed into a vacuum chamber that forms the second part. This is where the pulse is transformed from 800 nm to light in the x-ray regime by HHG and then propagates to the sample. See Fig. 3.3 for a schematic of the setup.

To generate the pulses, a mode-locked Titanium doped sapphire (Ti:sapphire) oscillator (Spectra Physics Tsunami), pumped by a continuous wave (CW) 532 nm Neodymium doped Yttrium Aluminium garnet (Nd:YAG) (Spectra Physics Millenia Vs), emits a broadband 35 fs pulse centered around 800nm. The light is guided into a Spectra Physics Spitfire amplifier, pumped with 527 nm light coming from a Neodymium doped Yttrium Nd:YLF CW laser (Coherent EVO-30). The outgoing beam has around 2.7W power with a pulse rate of 1 *kHz*, and passes through a shutter, an iris and a focusing lens before it enters the vacuum part of the setup.
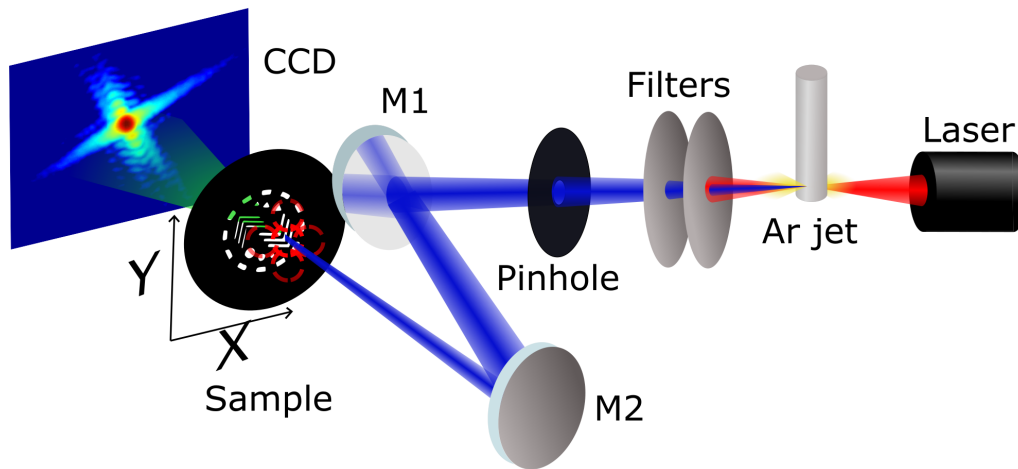
Figure 3.3: *Experimental setup for ptychography. The laser beam enters a vacuum where coherent x-rays are generated by HHG with an argon jet. The fundamental laser beam is filtered out and, stray reflections are blocked by an adjustable pinhole. Mirrors M1 and M2 select the 27th harmonic and M2 focuses the beam on a movable sample. The diffracted light is finally captured by a UV sensitive CCD camera*

3.2.1 HHG

Once the focused 800 nm beam is in the vacuum the high harmonics can be generated. Due to their interaction with matter, it is necessary that the remainder of the setup is under vacuum. The high harmonics are generated as the IR beam hits an argon gas jet by HHG as described in section 2.4. When a new capillary is inserted, the focused laser beam will drill a hole in the capillary. The capillary is wrapped in aluminium foil and Teflon tape to protect the newly drilled hole from growing in size. Since the jet is placed in a vacuum, it is important to keep the holes in the capillary as small as possible so that the gas flow from the jet is as low as possible while maintaining a pressure of around 7 Torr in the capillary. For the same reason, it is important to be careful with the pointing of the laser.

It is desirable to limit the integration times during the measurement, and therefore the x-ray beam must be as bright as possible. Several pa-

rameters can be tuned to generate a higher intensity beam: the pointing of the beam into the gas jet, the mode of the laser by changing the setting of the iris, the position of the focus to control the Gouy phase, the gas pressure of the jet, compression of the driving laser pulse, laser power and oscillator bandwidth. The best settings change slightly from day to day and every day the parameters were optimized in an iterative fashion.

A 200 nm parylene, coated with aluminium, is located directly after the gas jet to filter the 800 nm light from the incoming laser beam to protect the CCD camera from the intense light. A second filter, in the form of a filter wheel with multiple 200 nm Al filters with different coatings, is located further downstream with a toroidal mirror between it and the first filter. The mirror is used to focus the beam since lenses can't be used for soft x-rays. Once the beam enters the imaging chamber, the beam is reflected by two coated mirrors that act as a monochromator where only the 27*th* high harmonic with a wavelength of 29.5nm is reflected. The second mirror is curved with a focal length of 30 cm and focuses the x-rays on the sample. Finally, the light passes through the sample and 9.5 cm further the diffraction patterns are captured by a cooled 16-bit 2048 $\times$ 2048 CCD camera (Andor iKon-L) with pixels of 13.5μm by 13.5μm. The camera was typically cooled down to $-70^\circ C$ to eliminate thermal noise.

Before the measurement can start, the 150μm sample has to be put in place so that the 20μm beam is roughly centered on the sample, but the x-ray probe can only be used under vacuum. Since it is very difficult to find the sample in these conditions, it was first centered by using a HeNe laser that is used to align the setup. In this way the center is much easier to find as the beam is visible and of a much higher intensity than the x-ray beam. Once the aperture of the sample was found the imaging chamber could be pumped down to find the center for the x-ray beam, which is often very close to the HeNe beam, after which the measurements could start.

The sample is mounted on a stack of different stages which move the sample during the measurement. One stage is open loop with a large

range and is used to move the sample in and out of the beam. Since the x-rays beam has to be optimized at least every day, having such a stage means that the setup can remain under vacuum as the sample does not have to be taken out and can simply be moved to the side. Three other close loop stages (Attocube ANPx101) can move the sample in all three dimensions with 1 μm accuracy, stable within 300 nm, and are used for scanning over the ptychography raster. The readout of the positions of the motors is very accurate, but there still is some degree of backlash present in the translation steps of the motors. We discovered that translations in the y-direction are more accurate when the sample only goes down during the scan, probably due to the weight of the other stages and the sample, and therefore the scan is a zig-zag going from left to right, then down a step, and then from right to left, etc. It is no problem if the real positions deviate from the programmed positions: as long as the real positions are recorded accurately, it will prevent periodical artifacts from forming in the reconstruction [34].

The size of the beam waist at the focus, roughly at the position of the sample, was estimated to be 20 μm. An overlap of at least 70% should result in good reconstructions [47, 34, 48], and , the step size needed to be $4\mu m$ or smaller. Although the stages can move within $1\mu m$ accuracy, this is only true for steps larger than $3\mu m$. This puts a limit on the minimum step size for the raster and thus on the maximum degree of overlap too. For this reason it was not possible to eventually increase the degree of overlap beyond 70% in the search for a higher resolution.

One requirement, maybe the most important one to get a good reconstruction, is that the beam of the probe needs to be as coherent as possible, while it also helps a lot when the beam approximates a Gaussian as this allows to start with a better guess of the probe. For that reason a pinhole was placed in the beam, such that blocks incoherent scattered background light and only lets the central, Gaussian part of the beam through. Without this pinhole, a large area outside of the main beam that consists of incoher-

ent scattered light will also hit the sample an results in blurred diffraction patterns that are difficult or even impossible to reconstruct.

3.2.2 Reconstruction

As for CDI, multiple images were recorded per position and averaged during the pre-processing. Noise that originated from the detector is removed by subtracting background images from the diffraction patterns. Before the ptychography scans were started, background images were taken at a single position, since the only goal is to capture any background light that is present. These images are weighted according to the ratio of background images to diffraction patterns per position and then subtracted from these diffraction patterns. The pre-processing code also has an option to apply a Gaussian filter and to stitch high and low exposure diffraction patterns, similar to the CDI pre-processing code.

Because ptychography data sets are much larger than for CDI after the pre-processing is done, the diffraction patterns are cropped to make it computationally less intense during the reconstruction. Only the parts that do not contain any information can be cropped, as otherwise the resolution will decrease as the high-angle information is removed. At the same time the cropping is used to center the diffraction patterns with an accuracy of a few pixels. This proved to be very important for the reconstruction as it prevents the reconstruction of the probe to drift around.

The actual reconstruction process closely follows the ePIE methods as explained in section 2.3.1. The probe is not updated in the first few iterations, it is suggested in the literature that this helps the algorithm to find the global minimum [34]. A variation on this is to make multiple guesses for the initial probe and refine them for a few iterations as if it were the only guess. After that the refined probes are averaged and this is then refined further by a few (1 to 5) more ePIE iterations. The resulting probe function is then used as initial guess for the reconstruction of the object and should make the process faster, but above all, more stable [35, 34]. The

reconstruction algorithm continues to refine the probe and object function from this point until a pre-specified number of iterations or error tolerance is reached.

3.2.3 Resolution

To quantify the quality of the reconstruction, the resolution needs to be determined. One way of doing this is to look at the amplitude of the pixels over a line, preferably at the center of the reconstruction as the quality at the edges will be lower due to a lower redundancy of information. However, this does not mean that the resolution of the whole image is lower, i.e. if the scan size would have been larger the resolution in the same area might be much higher. The resolution is then determined as the distance between 10% and 90% of the maximum pixel value. Ideally, there is a plateau where several pixels have the same maximum value which is necessary to determine if the pixels indeed have there saturation value. Although this method remains slightly arbitrary as where to take the scan, and does not make reliable estimate of the resolution when the quality of the reconstruction is inhomogeneous, it can give a good indication of the reconstruction quality in this stage where pixel limited resolution is still far away.

Chapter 4

Results and discussion

4.1 CDI

The CDI measurement was performed on a very compact and simple setup, as was described in section 3.1. In order to minimize errors induced by thermal effects, 400 images, which are an average of 10 images themselves, were taken for each exposure time. These were determined by checking when the detector gets saturated. In order to be sure that the measurements done with the low exposure time are indeed unsaturated, it was chosen at 60% of the time it takes to slightly saturate the detector. The high exposure time should be long enough so that the center, i.e. the zeroth and first order peaks, of the image is completely saturated while at the edges of the detector clear features are visible. For this particular experiment the short and long exposures were 3ms and 30ms respectively. To correct for background noise, another 400 images were taken for each exposure time with the laser turned off so that they could later be subtracted from the other images.

Since the reconstruction software is able to make reconstructions in the near field too due to the inclusion of the distorted object, the sample was placed at a distance of 3.5 cm which implies a Fresnel number of $F_n = 1,02$ for this sample and wavelength, meaning that the sample is in the near

38

field. These settings result in an oversampling ratio of 28, safely above the minumum oversampling ratio of 2.

All these images were then processed to form one composite image that can be used to make the reconstruction. The pre-processing program first sums all the images of both exposure times separately and continues with the averaged image which are then stitched together, according to the method described in section 3.1. The threshold level at which the long exposure time image is cut is 65%, so that we can be sure that the camera still was in its linear regime at those points. After the image is smoothend and centered it is ready to be reconstructed.

a)   b)
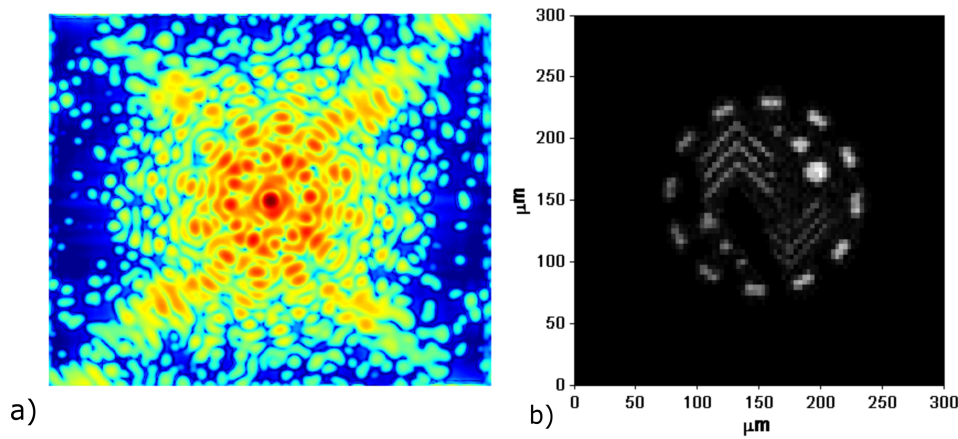
Figure 4.1: *a) shows a logarithmic picture of the reconstruction pattern that was used to make the reconstruction, of which a cropped version is displayed in b). The pixels in the object reconstruction are clearly visible, showing that the resolution is pixel limited.*

As was mentioned before, the reconstruction program uses a combination of three reconstruction algorithms: The error-reduction algorithm, the hybrid input-output algorithm and the shrink wrap algorithm. This results in a faster convergence and a better resolution than when only one of these algorithms is used. For the reconstruction shown in Fig. 4.1, 5 ER iterations were followed by 20 HIO loops and one shrink-wrap loop,

which in total form a single reconstruction loop. Since $F_n \approx 1$, the Fraunhofer approximation can't be used and therefore a distorted phase object was included in the ER and HIO algorithm. This loop is then continued until a specified number is reached or when the error is lower than a specified threshold. In this case the reconstruction was run for 50 loops and followed up by another 100 ER loops to increase the quality of the reconstructed image. A full reconstruction takes on the order of a few minutes on a modern computer.

The resolution of the reconstruction in Fig. 4.1 b) is difficult to determine since the individual pixels are visible, and therefore it is not justifiable to take the distance between 10% and 90% of the maximum intensity as its resolution. By noting that the smallest features of the test sample, namely the smallest triangle and circle, are $3\mu m$, one can conclude that since these features are still resolvable the resolution is roughly $3\mu m$, and limited by the number of pixels that in the sample plane are of the same size. A solution to obtain better solutions with the same setup would be to place the sample closer to the detector and thereby decreasing the oversampling, but at the same time also decreasing the pixel size in the sample plane according to Eq. 2.15. Additional to this effect one can also capture scattered light at much higher angles that help to resolve the smaller features, provided that the intensity is still high enough to detect the light at these angles. The lower oversampling ratio and the fact that these measurements are taken in the very near field will make it more difficult to get faithful reconstructions though.

4.2   Ptychography

After the successful reconstruction of the test sample by using CDI it was placed in the setup described in section 3.2 to capture images that can be reconstructed by the ePIE algorithm. During the reconstructions of the first measurements it became apparent that the data was not of a quality

high enough for reconstruction, due to scattered light entering the imaging chamber of approximately 10% of the intensity of the maximum of the x-ray beam. The origin of this light is somewhere earlier in the setup, where the light got scattered and consequently is not coherent anymore. To filter out as much of the stray light a pinhole was put in place in the imaging chamber so that only the coherent Gaussian beam could propagate to the sample. The result of this minor but important modification is shown in Fig. 4.2, which shows the diffraction pattern originating from the chevrons in the sample. The fringes are clear and distinct, opposed to the situation before where the diffraction pattern was not much more than a continuous blob where no features were distinguishable. By shining the filtered beam directly on the detector it could be verified that indeed most, but not all, of the stray light was blocked by the pinhole, leaving a beam with a diameter of roughly $20\mu m$ at the position of the sample.
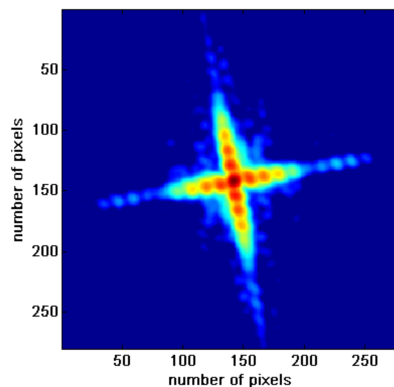
Figure 4.2: *An example of a diffraction pattern at one position a ptychography scan.*

Once the pinhole was put in place, the first reconstructions could be made. Since all the correct parameters for the setup had yet to be found, a relatively small scan of $60\mu m \times 60\mu m$ was used so that one still can be sure that some of the features of the sample will be captured within the scanned raster. An overlap of 70% between two neighbouring positions of the beam was used, a value that has been found to still give reliable

results [34, 48]. Although it is close to the lower limit, it also allows to do measurements more quickly after each other, something that is advantageous in this stage. Besides that, the step size is limited by the accuracy of the piezo stages that move the sample around. Although the stages are close-looped and are specified to be stable within $50nm$, in reality they showed to be considerably less accurate. Since the positions are accurately recorded as they are needed for the reconstruction, it is known that the position of the motor is drifting around up to $0.3\mu m$ where it should have stayed constant. While it is known that deviating from a perfect raster, provided that the positions are still accurately known, can prevent the formation of periodical artifacts. But it is important to note that, like in the CDI experiment, multiple images per position are taken while the position is only recorded once per position. Not only will this potentially result in a more blurred diffraction pattern, it is also possible that the average position of the four images is different than the recorded position, although this was not verified. To minimize the effects of drifting stages, the detector waited for two seconds after moving the stages to let them stabilize before taking pictures.

A different measure to limit the time needed for one measurement is to limit the number of pixels that are read out from the CCD detector. Due to the wavelength of $29nm$ and the intensity of the beam, no light is detected at higher angles and thus these pixels can be neglected without loss of information. For this measurement, 301×301 pixels were used. During the centering in the pre-processing, this was reduced by another 20 pixels in each direction to get the zeroth order beam at the center of the detector, after which the reconstruction was made. The result after 20 iterations is shown in Fig 4.3, the first-ever ptychographic reconstruction from this setup.

The reconstruction clearly shows the features of the sample, although it is more blurry at the edges due to a lower redundancy of data. The phase image of the object shows the same story, with a relative phase of 0 at the

transparent parts of the sample and $\pm\pi$ elsewhere. The reconstruction of the probe in 4.3 c) indeed shows a size close to $20\mu m$ but is not Gaussian and the areas with lower intensity is not uniform or even clearly cut of, which can be expected as the pinhole in the imaging chamber blocks the beam. Since the reconstruction of the object and the probe are coupled, it can be concluded that the reconstruction of the beam is probably close but not exact, since the object reconstruction did not yield a binary picture of the sample. The resolution of the reconstruction was obtained by using MATLABs pixel cross section tool along the red line in Fig. 4.3 a). The rectangle was chosen because it isn't close to the center and because it is a large feature, which is handy as it is more reliable to look for the resolution in this way when there is a plateau of high amplitudes.

After this successful reconstruction several other experiments were performed to see if the resolution could be increased and what the effects of overlap, raster size and the averaging of images on the resolution are. To start with, the scan size was increased so that the complete sample could be imaged, while the degree of overlap remained constant at 70%. Since the beam size is fixed in this experiment the only way to go is to take measurements at more points on the raster. One of the biggest challenges in large scans is that the pointing of the laser beam will change slightly over time. This effect is enhanced by changes in ambient conditions such as temperature and pressure, two variables that will inevitably change during a day. To limit the duration of the measurements the images were averaged over only four exposures and the CCD pixels were binned 2×2. The read-out time for the camera will decrease due to the binning, but it also changes the value at which the camera saturates. As such, the exposure time had to be decreased to 0,25s to keep the camera operating in the linear regime. At the same time, binning helps increasing the dynamical range of the camera. Binning of the pixels acts as a four time amplification, and despite the saturation value is only 2.5 times the saturation value of the single pixel readout, it means that after exposure times are corrected,

the camera is still more sensitive at higher angles where the diffracted light is less intense. For that reason, the number of 'artificial' pixels that were used are the same as before, but because they are binned it were actually twice as much and allow to capture light at higher angles. The result is shown in Fig 4.4, with a resolution of up to $3\mu m$ similar to the first reconstruction, despite the fact that the measurement took 6 hours to complete. It should be mentioned though that on average the resolution is much lower, the features are more blurred and the transparent parts have more structures in them.

Because the ePIE algorithm reconstructs the object- and probe function at the same time to reconstruct the exit wave, a bad reconstruction of the probe will result in a less than ideal reconstruction of the object. But as a result of the long duration of the measurements, it is not possible to simply reconstruct the probe, as it evolves over time. The ePIE algorithm is not able to handle this and will regardlessly try to make a single reconstruction for the probe, which explains the lower resolution as compared to the resolution of the reconstruction in Fig. 4.3. Compared to the probe from Fig 4.3 c), the reconstructed probe in Fig. 4.4 is larger although it is closer to a Gaussian beam, despite the real probe having the same size for both measurements. Something else that is noticeable in the reconstruction is that the circles appear to be rings. The reason for this is that the exposure time was too long and the the beam could, almost unobstructed, propagate through the circles and saturating the detector and therefore making the task of the reconstruction algorithm much harder.

Also the phase of the reconstructed light in Fig 4.4 b) shows that the algorithm had difficulty with resolving the apertures. The phase is still close to zero, but the same can be said for the edges and it is less clear than was the case for the previous reconstruction. It also shows that the chevrons are not resolved at all, something that is visible on the amplitude reconstruction too.

Since the time for one measurement was too long and the detector

was saturated at some positions of the scan, the scan size was reduced to $40\mu m \times 40\mu m$ and the exposure time was reduced to $0.15s$ while not binning the pixels anymore, a value at which the detector doesn't saturate even when the beam was aimed directly on it. The step size was decreased to $3.5\mu m$ so the overlap increased to 75% and in an attempt to capture light at higher angles than in the first experiments an array of 501×501 pixels was used with no binning. And finally the number of pictures per position were increased from four to ten. The results in Fig. 4.5 show that these measures have indeed helped to improve the resolution. The chevrons are clearly resolved again and the pixel value cross section shows that the resolution increased to $2\mu m$. The fact that the rectangles at the side are not reconstructed as well as the chevrons is because they are close to the edge of the scan. The probe is also much closer to the expected size of $20\mu m$, which is to be expected since it is coupled to the better object reconstruction. However, after the experiment it was found that due to a rise of temperature in the lab the beam has slightly drifted, which has probably compromised the quality of the reconstruction.

The final measurement is almost exactly identical to the previous one, except for that the position of the sample was different this time, because the the algorithm sometimes has difficulty in resolving periodic features such as the chevrons when no or little other features are present. However, this time the detector was only cooled down to $20°$ C instead of $70°$ C. The reconstruction in Fig. 4.6 looks good, but especially the phase reconstruction makes it clear that the triangles seem to have drifted, leaving phase ramps visible in the construction where it should have stayed constant. An important reason for this is that the thermal noise in the diffraction images has increased significantly over the level of the previous three measurements, which is difficult to remove during pre-processing without cutting of real data too. The result is that the resolution, despite still being better than in the first measurement, slightly decreased, being around $2.5\mu m$ now.
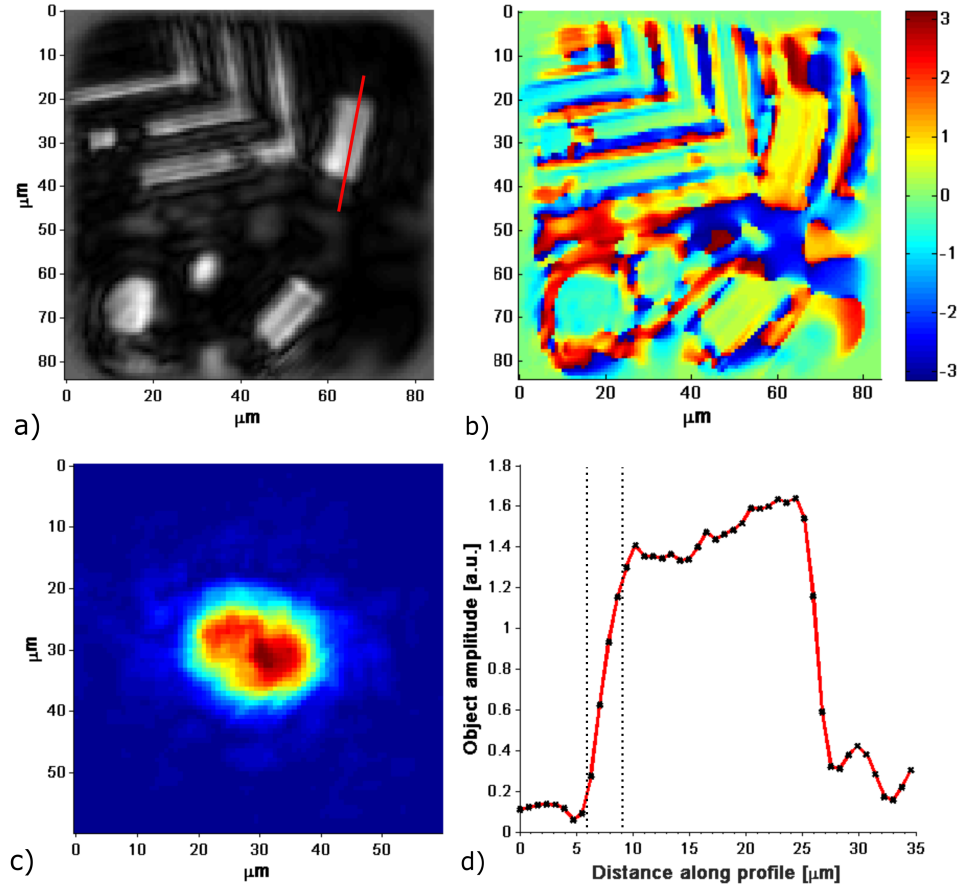
Figure 4.3: *Results from the ptychographic reconstruction from a $60\mu m \times 60\mu m$ scan with 70% overlap. Fig. a) shows the amplitude of the object reconstruction; b) is the object phase. c) shows the reconstruction of the x-ray probe. Fig d) shows the cross section values from the red line in a), where the resolution was determined to be $3\mu m$*
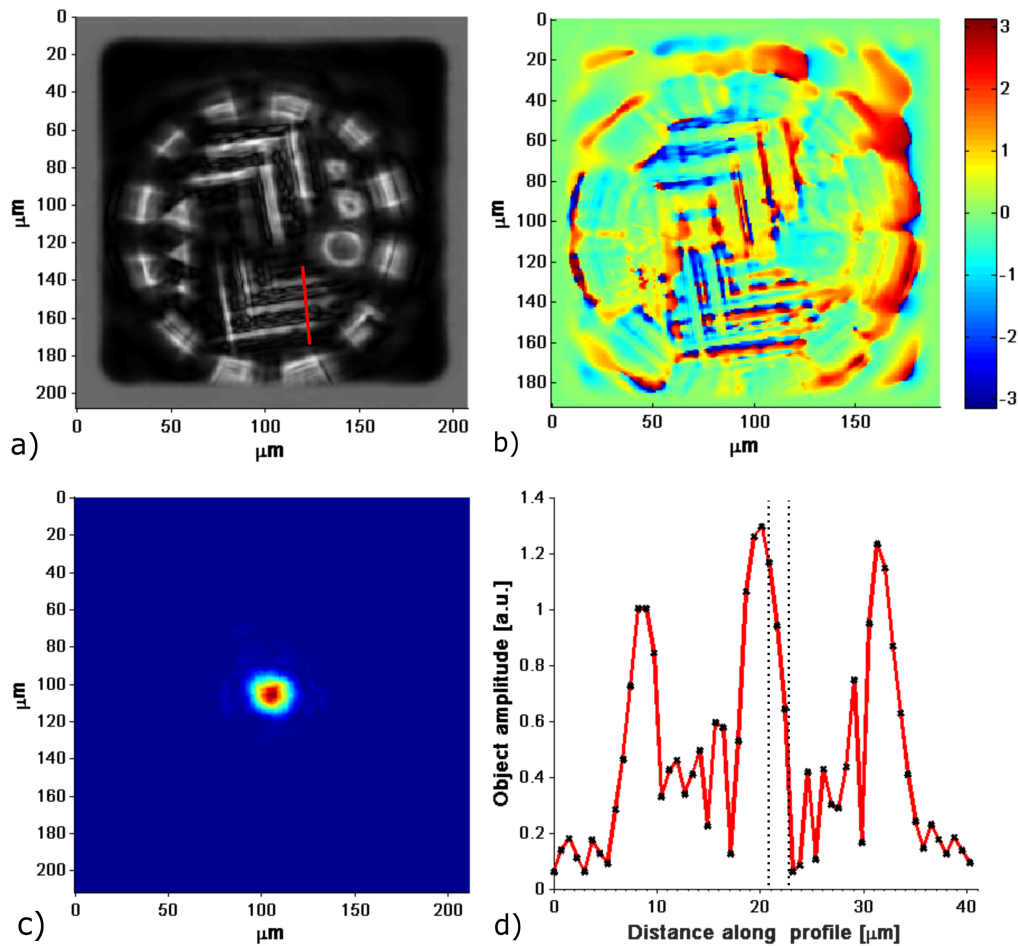
Figure 4.4: *Results from the ptychographic reconstruction from a $160\mu m \times 160\mu m$ scan with 70% overlap and 2×2 binning of the pixels. Fig. a) shows the amplitude of the object reconstruction; b) is the object phase. c) shows the reconstruction of the x-ray probe and d) shows the cross section values from the red line in a), where the resolution was determined to be $3\mu m$*
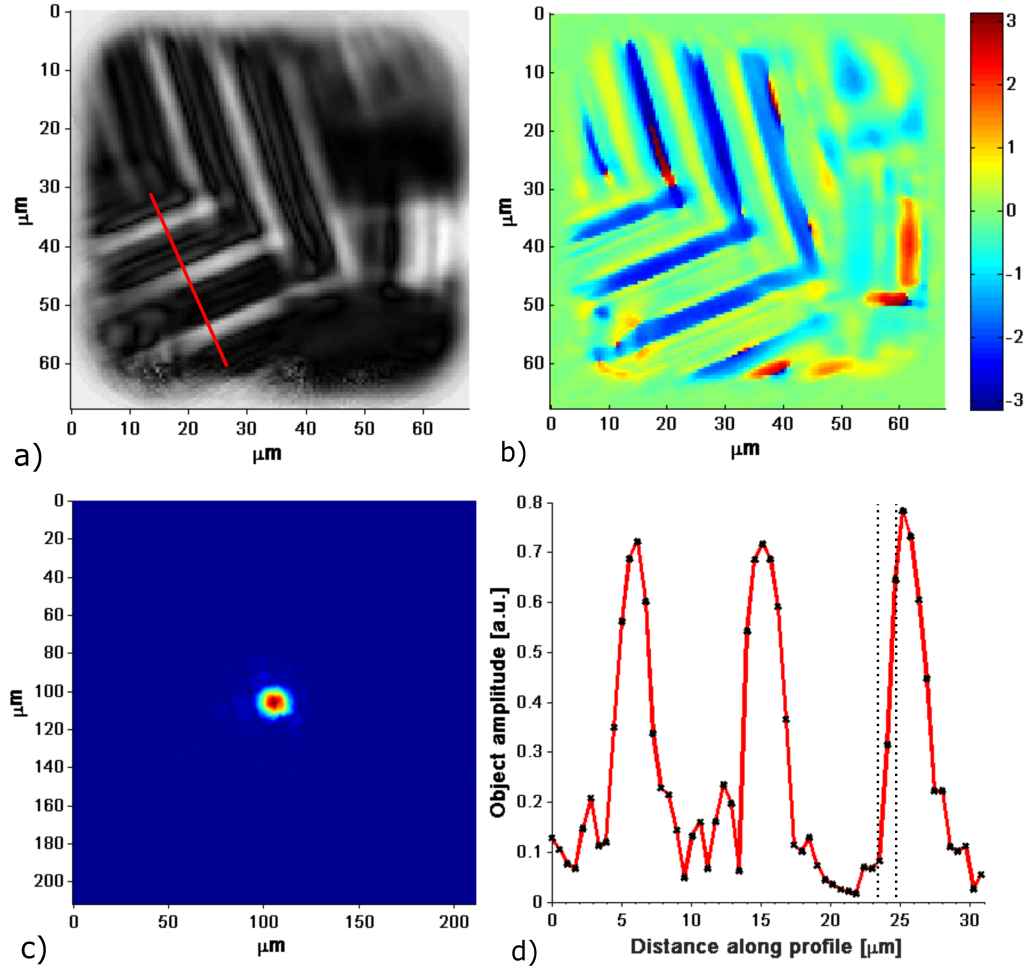
Figure 4.5: *Results from the ptychographic reconstruction from a $40\mu m \times 40\mu m$ scan with 75% overlap. Fig. a) shows the amplitude of the object reconstruction; b) is the object phase. c) shows the reconstruction of the x-ray probe, d) shows the cross section values from the red line in a), where the resolution was determined to be $2\mu m$*
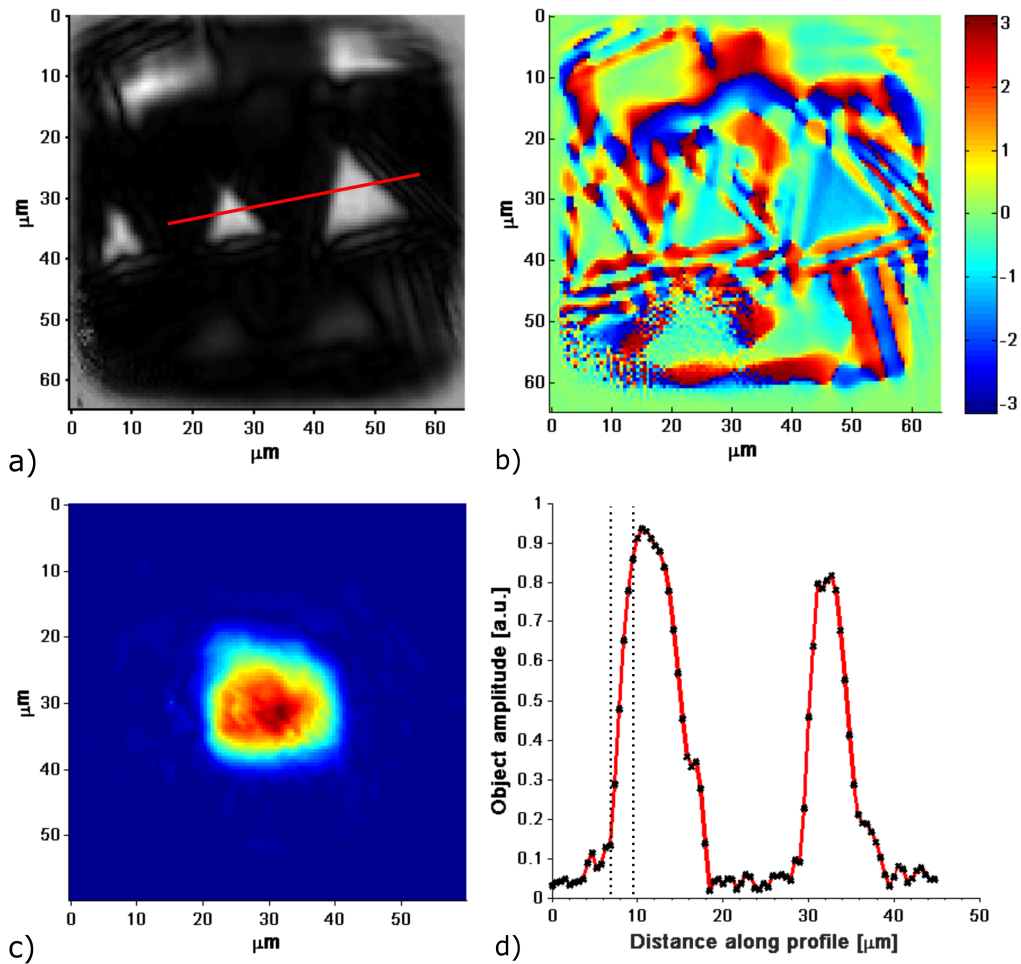
Figure 4.6: *Results from the ptychographic reconstruction from a $40\mu m \times 40\mu m$ scan with 75% overlap. Fig. a) shows the amplitude of the object reconstruction; b) is the object phase. c) shows the reconstruction of the x-ray probe, d) shows the cross section values from the red line in a), where the resolution was determined to be $2.5\mu m$*

Chapter 5

Discussion

From the reconstructions in the previous chapter we can see that certain aspects such as a low detector temperature and a sufficiently large pixel area are important to get good resolution images. However, even if the resolution will improve by a factor of two, it is still far away from a resolution set by the wavelength of the probe. One thing that is relatively easy to improve is the quality of the beam. The pinhole that was used in the experiments was slightly too large, not only letting through the beam but also still a part of the scattered light. A solution to this is to use a smaller pinhole that slightly clips the beam edge, and putting another pinhole after that blocks the light that is scattered from the first pinhole [49].

Only a small portion of the pixels has been used as no light could be detected at larger angles without saturating the central pixels. The obvious solution would be to stitch the images like in the CDI measurement, which will greatly improve the dynamical range of the camera. A drawback of this solution is that it will take longer and therefore the pointing of the beam and the position of the sample have to be more stable than before.

On the software side some other improvements can be made. It is already very common to use sub pixel centering, an extension to ePIE, for the diffraction images, which counterbalances the variation of the pointing of the beam [50]. Instead of centering the whole collection of diffraction

50

patterns only in the beginning with a few pixels accuracy, this can be done iteratively with improved centering in each step up to values smaller than the pixel size, and is done for every probe position. At the same time, this method is able to extract the exact position of the sample relative to the beam, which is used to largely eliminating the effect of the beam moving over time [50].

What is also unknown is what the beam exactly looks like at the sample, and therefore the initial guess of the beam is probably far off from the real beam. Instead of the plane wave Gaussian beam that was used for the initial guess, it is almost guaranteed that the real probe has a curved wave front at the sample. Only when the sample is exactly in the focus this might be a good estimate, but this is not the case outside the focus and in that case a curved wavefront would be a better first guess. Besides that, the beam is astigmatic to some degree due to the toroidal mirror that is used to focus it, again something that was not included in the initial guess. For that reason the beam itself will need to be characterized thoroughly so the algorithm can correct for it. Most of these proposed improvements have already been used in an experiment by Baksh *et al.* in 2016, who published results from the first ptychographic reconstruction in transmission geometry and obtained a resolution of 56 nm [47].

In terms of intensity there is a lot to win by moving to broadband ptychography. While people are trying hard to get as much light as possible from HHG setups, most of the light is thrown away as only one single harmonic is used for the probe. One solution to this is ptychographical information multiplexing (PIM), which has already shown to work in a proof-of-concept in the visible range and more recently in the soft x-ray range too, although these measurements are done in reflection geometry [51, 52]. Instead of a coherent diffraction pattern, an incoherent diffraction pattern is captured due to the multiple wavelengths that are used. By using a modified version of the ePIE algorithm, the redundancy of data that comes along with a ptychography measurement can be used to resolve the

coherent diffraction patterns from the incoherent one for each wavelength. Instead of updating a single object and probe function, a multiple of them are now updated in parallel, while in addition a relative weighting for the intensity of each illumination wavelength is recovered too.

5.1   Outlook

One of the most exciting developments in the table top lensless imaging is its application in materials science, especially in the research of magnetic properties of ferromagnets Fe, Co and Ni. Their magnetic properties are determined by the valence electrons that fill the 3d shell. They become increasingly filled for these respective materials, resulting in a decreasing number of holes where electrons from lower shells can be excited to. The net magnetization is a result of the exchange interaction between the valence electrons, resulting in a difference in number of electrons with spin up and with spin down. To measure the properties of these electrons, a probe that is spin dependent is needed, such as the circularly polarized light that is used in x-ray magnetic circular dichroism (XMCD), which can for example be used to image the ferromagnetic domains [53]. The circularly polarized photons can transfer their angular momentum to an electron from the p band, which carries it as spin and / or angular momentum.

   Fig. 5.1 illustrates the origin of spin dependent absorption. In the case where no linearly polarized light is used (Fig. 5.1 a), there is no mechanism that differentiates between spin up or down and an electron from the p-band simply gets excited to the d-band. Because of spin-orbit coupling, the p band does actually exist of two levels separated in energy. The $p_{3/2}$ L_3 level is highest in energy, where the z component of the total angular momentum $j = l + s = 3/2$. The $p_{1/2}$ L_2 level on the other hand has a lower energy, with $j = l - s = 1/2$. The light exciting the photoelectrons is absorbed at the energy difference between the free 3d band states and the L_3 and L_2 levels, resulting in two peaks in the absorption intensity

spectrum, where the total intensity of the two peaks together is directly proportional to the number of free 3d states.

When circularly polarized light is used, the process becomes spin dependent. Fig. 5.1 b) illustrates absorption for right and left circular polarized light (RCP and LCP, respectively), which carry opposite angular momentum. When circularly polarized light excites the electrons, a two step process takes place [54]: in the first step the circularly polarized light transfers its momentum, either $\hbar$ or $-\hbar$, to the electron, which can be transferred either partly or completely to the spin through spin-orbit coupling. Because RCP and LCP light transfer opposite angular momentum, photoelectrons are created with opposite spins in the two cases. Due to opposite spin-orbit coupling for the L_3 and the L_2 levels, the spin polarization will be opposite at these edges. In this process, spin up and spin down are defined relative to the photon helicity, which is parallel (RCP) or antiparallel (LCP) to the x-ray propagation direction [54]. In the second step the spin-split valence shell acts as a detector for the spin state of the photoelectrons, and this is where the magnetic properties enter in the process. An important rule is that spin-flips are forbidden during the transition from the p to the d-band, so that spin-up electrons can only get excited to spin-up hole states. This means that the probability of an electron getting excited now is proportional to the spin-dependent number of free 3d hole states available. The quantization axis of the absorption is given by the magnetization direction, and this is why peak A and B, from the L_3 and the L_2 edge respectively, are of oppisite sign due to their opposite spin-orbit coupling. By determining the intensities of the L_3 and L_2 peaks for both polarizations, one can obtain quantitative information about magnetization of the sample with the help of sum rules [55]. If this scheme is applied for every scanning position during a ptychography measurement, it can result in an image of areas of different magnetization. Up until now, these kinds of measurements have only been done at synchrotron facilities and with hard x-rays [56, 57] and it is not yet successfully done on tabletop
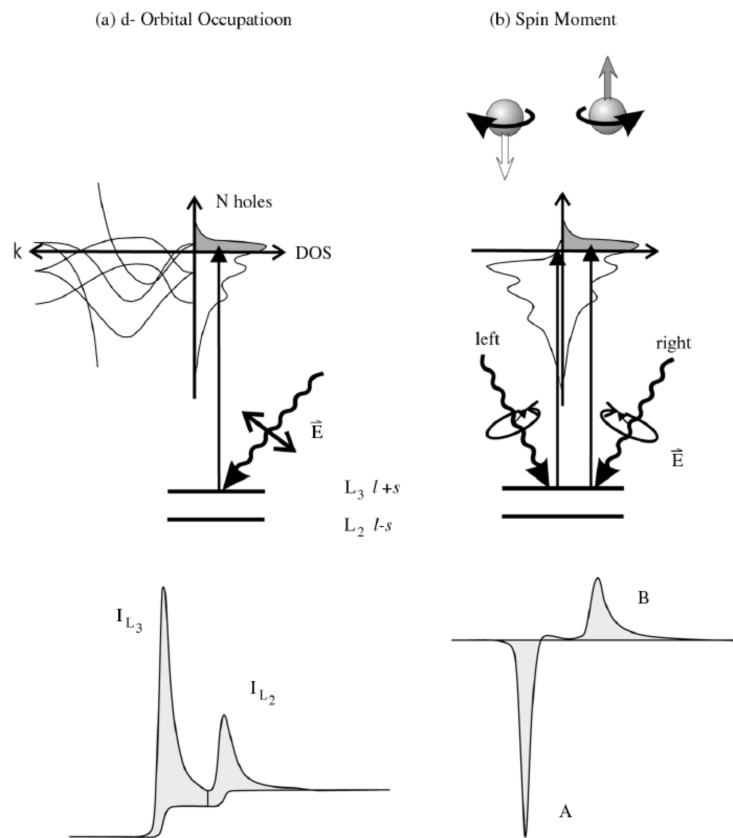
Figure 5.1: *a) shows the excitation of an electron in conventional L-edge x-ray absorption. b) illustrates the x-ray magnetic circular dichroism from the 2p shell that is split due to spin-orbit coupling. [54]*

setups. The challenges that will need to be overcome are the low intensities compared to synchrotrons, as well sample preparation. Although soft x-rays give better XMCD signals than hard x-rays [58], the samples have to be very thin ($< 100nm$) in order to still be able to capture light. Besides, it is hard to make high quality circular polarized light from a HHG setup as waveplates cannot be used for soft x-rays and the HHG process will be less efficient when wave plates are put in front [59]. However, these developments show that there's definitely the possibility that table top ptychography can play a role in research of magnetic properties in the future.

Chapter 6

Conclusion

Optical instruments have been important in many areas of science. They allow us to take a look in the microscopic world that forms the building blocks of our own macroscopic one. But when scientists zoom in further and further, they run into problems as the resolution of optical microscopes is limited by the wavelength of the light that is used. Using light with a shorter wavelength, such as soft x-rays, can help in the search of higher resolution microscopes. However, conventional optics are opaque to x-rays and therefore other methods are needed to replace the role of the traditional lenses which convert the diffracted light into a magnified image of the object.

Coherent diffraction imaging is one of these methods, where a relatively large beam illuminated the object and the captured diffraction pattern can be reconstructing by iterative algorithms. By using light with a wavelength of 633nm, an $80\mu m$ beam illuminated a binary test sample with features of different sizes was illuminated and the diffraction pattern was captured with $F_n = 1$. The resolution of the image is limited by the number of pixels at $3\mu m$, measurements closer to the near field are needed for higher resolution images.

The same sample was then used for Ptychography measurements, where a soft x-ray beam with a wavelength of 29 nm acted as a probe. Instead of

55

using a single position for the beam, the beam is scanned over the sample while overlapping with adjacent positions. The diffraction patterns were reconstructed with the ePIE algorithm, resulting in object reconstructions with a resolution up to $2\mu m$.

Acknowledgements

First of all, I want to thank Ron Tobey for asking me if I wanted to do my master's research in his group. Thank you for giving me this great opportunity and for the internship you arranged at the Los Alamos National Laboratory. I learned a lot during this project, both in general and physics related. And secondly, I would like to thank Richard Sandberg for working together with Ron to organize the internship. I know you did a lot of work to arrange everything for me there. I'm very grateful that you took the time to show me my way around Los Alamos and at the lab, and took the time to explain me how to work with the setup. I also want to thank all the people from the OCMP group, especially Qi Liu for teaching me how to work in a laser lab. It was an enjoyable experience working in the group. And thanks to Yanxi Zhang and Jamo Momand for helping me with fabricating and characterizing my samples.

From the people in Los Alamos, I want to especially mention Ben Pound and Brian McFarland. You were both very important for my project and always took time to explain the setup or reconstruction codes to me when I was stuck again. Besides that, it was great to talk with you in general about non-physics subjects. And of course thanks to all the people of the LUMOS group and CINT at LANL who helped me during my project.

Bibliography

[1] F. Zernike, *Phase contrast, a new method for the microscopic observation of transparent objects part II*, Physica **9**, 686 (1942).

[2] F. Zernike, *Observation of Transparent Objects*, Physica , 974 (1942).

[3] E. Ruska, *microscopy*, Reviews of Modern Physics **59** (1987).

[4] G. Binnig, H. Rohrer, C. Gerber, and E. Weibel, *Tunneling through a controllable vacuum gap*, Applied Physics Letters **40**, 178 (1982).

[5] E. Betzig, G. H. Patterson, R. Sougrat, O. W. Lindwasser, S. Olenych, J. S. Bonifacino, M. W. Davidson, J. Lippincott-Schwartz, and H. F. Hess, *Imaging intracellular fluorescent proteins at nanometer resolution.*, Science (New York, N.Y.) **313**, 1642 (2006).

[6] S. W. Hell and J. Wichman, *Breaking the diffraction resolution limit by stimulated emission: stimulated-emission-depletion fluorescence microscopy*, Optics Letters **19**, 780 (1994).

[7] R. M. Dickson, a. B. Cubitt, R. Y. Tsien, and W. E. Moerner, *On/off blinking and switching behaviour of single molecules of green fluorescent protein.*, Nature **388**, 355 (1997).

[8] J. W. Goodman, *Introduction to Fourier Optics*, McGraw-Hill Series in Electrical and Computer Engineering: Communications and Signal Processing, McGraw-Hill, 1996.

[9] J. Peatross and M. Ware, *Physics of Light and Optics*, Brigham Young University, 2008.

[10] C. Kisielowski et al., *Detection of single atoms and buried defects in three dimensions by aberration-corrected electron microscope with 0.5-A information limit.*, Microscopy and microanalysis the official journal of Microscopy Society of America Microbeam Analysis Society Microscopical Society of Canada **14**, 469 (2008).

[11] N. C. I. Raméntol, *Transmission electron microscopy in cell biology: sample preparation techniques and image information*, Capítol del llibre: … (2012).

[12] G. J. Williams, E. Hanssen, A. G. Peele, M. A. Pfeifer, J. Clark, B. Abbey, G. Cadenazzi, M. D. De Jonge, S. Vogt, L. Tilley, and K. A. Nugent, *High-resolution X-ray imaging of Plasmodium falciparum-infected red blood cells*, Cytometry Part A **73**, 949 (2008).

[13] W. Chao, B. Harteneck, J. Liddle, E. Anderson, and D. Attwood, *Soft X-ray microscopy at a spatial resolution better than 15 nm*, Nature **435**, 1210 (2005).

[14] E. Hecht, *Optics*, Addison-Wesley, 2002.

[15] D. Sayre, *Some implications of a theorem due to Shannon*, Acta Crystallographica **5**, 843 (1952).

[16] J. Miao, D. Sayre, and H. N. Chapman, *Phase retrieval from the magnitude of the Fourier transforms of nonperiodic objects*, Journal of the Optical Society of America A **15**, 1662 (1997).

[17] J. Miao and D. Sayre, *On possible extensions of X-ray crystallography through diffraction-pattern oversampling*, Acta Crystallographica Section A: Foundations of Crystallography **56**, 596 (2000).

[18] National Instruments, *Aliasing*.

[19] M. Hayes, *The reconstruction of a multidimensional sequence from the phase or magnitude of its Fourier transform*, IEEE Transactions on Acoustics, Speech, and Signal Processing **30**, 140 (1982).

[20] Y. Bruck and L. Sodin, *On the ambiguity of the image reconstruction problem*, Optics Communications **30**, 304 (1979).

[21] R. L. Sandberg, *Closing the Gap to the Diffraction Limit: Near Wavelength Limited Tabletop Soft X-Ray Coherent Diffractive Imaging*, PhD thesis, University of Colorado, 2009.

[22] R. W. Gerchberg and W. O. Saxton, *A practical algorithm for the determination of phase from image and diffraction plane pictures*, Optik **35**, 237 (1972).

[23] R. E. Burge, *Computer techniques for image processing in electron microscopy by W. O. Saxton*, Scanning **4**, 159 (1981).

[24] J. R. Fienup, *Reconstruction of a complex-valued object from the modulus of its Fourier transform using a support constraint*, Journal of the Optical Society of America A **4**, 118 (1986).

[25] J. R. Fienup, *Phase retrieval algorithms: a comparison*, Applied Optics **21**, 2758 (1982).

[26] S. Marchesini, H. He, H. N. Chapman, S. P. Hau-Riege, A. Noy, M. R. Howells, U. Weierstall, and J. C. H. Spence, *X-ray image reconstruction from a diffraction pattern alone*, Phys. Rev. B: Condens. Matter Mater. Phys. **68**, 140101/1 (2003).

[27] S. Marchesini, *A unified evaluation of iterative projection algorithms for phase retrieval*, Review of Scientific Instruments **78** (2007).

[28] X. Xiao and Q. Shen, *Wave propagation and phase retrieval in Fresnel diffraction by a distorted-object approach*, Physical Review B - Condensed Matter and Materials Physics **72**, 1 (2005).

[29] R. Suman, G. Smith, K. E. A. Hazel, R. Kasprowicz, M. Coles, P. O'Toole, and S. Chawla, *Label-free imaging to study phenotypic behavioural traits of cells in complex co-cultures.*, Scientific reports **6**, 22032 (2016).

[30] X. Shi, P. Fischer, V. Neu, D. Elefant, J. C. T. Lee, D. A. Shapiro, M. Farmand, T. Tyliszczak, H. W. Shiu, S. Marchesini, S. Roy, and S. D. Kevan, *Soft x-ray ptychography studies of nanoscale magnetic and structural correlations in thin SmCo5 films*, Applied Physics Letters **108** (2016).

[31] A. Ciani, M. Guizar-Sicairos, A. Diaz, M. Holler, S. Pallu, Z. Achiou, R. Jennane, H. Toumi, E. Lespessailles, and C. M. Kewish, *Segmentation of nanotomographic cortical bone images for quantitative characterization of the osteoctyte lacuno-canalicular network*, XRM 2014: Proceedings of the 12th International Conference on X-Ray Microscopy **1696**, 020040 (2016).

[32] T. B. Edo, D. J. Batey, A. M. Maiden, C. Rau, U. Wagner, Z. D. Pe??i??, T. A. Waigh, and J. M. Rodenburg, *Sampling in x-ray ptychography*, Physical Review A - Atomic, Molecular, and Optical Physics **87**, 1 (2013).

[33] P. Thibault, M. Dierolf, O. Bunk, A. Menzel, and F. Pfeiffer, *Probe retrieval in ptychographic coherent diffractive imaging*, Ultramicroscopy **109**, 338 (2009).

[34] A. M. Maiden and J. M. Rodenburg, *An improved ptychographical phase retrieval algorithm for diffractive imaging*, Ultramicroscopy **109**, 1256 (2009).

[35] J. M. Rodenburg and H. M. L. Faulkner, *A phase retrieval algorithm for shifting illumination*, Applied Physics Letters **85**, 4795 (2004).

[36] H. N. Chapman and K. a. Nugent, *Coherent lensless X-ray imaging*, Nature Photonics **4**, 833 (2010).

[37] A. McPherson, G. Gibson, H. Jara, U. Johann, T. S. Luk, I. a. McIntyre, K. Boyer, and C. K. Rhodes, *Studies of multiphoton production of vacuum-ultraviolet radiation in the rare gases*, Journal of the Optical Society of America B **4**, 595 (1987).

[38] T. Brabec and F. Krausz, *Intense few-cycle laser fields: Frontiers of nonlinear optics*, Reviews of Modern Physics **72**, 545 (2000).

[39] P. B. Corkum, *RevModPhys.72.545.pdf*, Physical Review Letters **71**, 1994 (1993).

[40] T. Popmintchev, M.-C. Chen, P. Arpin, M. M. Murnane, and H. C. Kapteyn, *The attosecond nonlinear optics of bright coherent X-ray generation*, Nature Photonics **4**, 822 (2010).

[41] H. C. Kapteyn, M. M. Murnane, and I. P. Christov, *Extreme nonlinear optics: Coherent X rays from lasers*, Physics Today **58**, 39 (2005).

[42] K. Varjú, P. Johnsson, J. Mauritsson, A. L'Huillier, and R. López-Martens, *Physics of attosecond pulses produced via high harmonic generation*, American Journal of Physics **77**, 389 (2009).

[43] P. Salières, A. L'Huillier, and M. Lewenstein, *Coherence control of high-order harmonics*, Physical Review Letters **74**, 3776 (1995).

[44] D. T. Attwood, *Soft X-rays and Extreme Ultraviolet Radiation: Principles and Applications*, Cambridge University Press, 2000.

[45] R. A. Bartels, A. Paul, H. Green, H. C. Kapteyn, M. M. Murnane, S. Backus, I. P. Christov, Y. Liu, D. Attwood, and C. Jacobsen, *Generation of Spatially Coherent Light at Extreme Ultraviolet Wavelengths*, **297**, 376 (2002).

[46] J. Miao, P. Charalambous, J. Kirz, and D. Sayre, *Extending the methodology of X-ray crystallography to allow imaging of micrometre-sized noncrystalline specimens*, Nature **400**, 342 (1999).

[47] P. D. Baksh, M. Odstrčil, H.-S. Kim, S. a. Boden, J. G. Frey, and W. S. Brocklesby, *Wide-field broadband extreme ultraviolet transmission ptychography using a high-harmonic source*, Optics Letters **41**, 1317 (2016).

[48] M. D. Seaberg, B. Zhang, D. F. Gardner, E. R. Shanblatt, M. M. Murnane, H. C. Kapteyn, and D. E. Adams, *Tabletop nanometer extreme ultraviolet imaging in an extended reflection mode using coherent Fresnel ptychography:supplementary material*, Optica **1**, 39 (2014).

[49] M. D. Seaberg, *Nanoscale EUV Microscopy on a Tabletop : A General Transmission and Reflection Mode Microscope Based on Coherent Diffractive Imaging with High Harmonic Illumination*, Thesis (2014).

[50] F. Zhang, J. Vila-Comamala, A. Diaz, F. Berenguer, R. Bean, B. Chen, A. Menzel, I. K. Robinson, and J. M. Rodenburg, *Translation position determination in ptychographic coherent diffraction imaging*, Optics Express **21**, 13592 (2013).

[51] D. J. Batey, D. Claus, and J. M. Rodenburg, *Information multiplexing in ptychography*, Ultramicroscopy **138**, 13 (2014).

[52] B. Zhang, D. F. Gardner, M. H. Seaberg, E. R. Shanblatt, C. L. Porter, R. Karl, C. A. Mancuso, H. C. Kapteyn, M. M. Murnane, and D. E. Adams, *Ptychographic hyperspectral spectromicroscopy with an extreme ultraviolet high harmonic comb*, Optics Express **24**, 18745 (2016).

[53] G. Schutz, W. Wagner, W. Wilhelm, P. Kienle, R. Zeller, R. Frahm, and G. Materlik, *Absorption of circularly polarized x rays in iron*, Physical Review Letters **58**, 737 (1987).

[54] J. Stohr, *Exploring the microscopic origin of magnetic anisotropies with X-ray magnetic circular dichroism (XMCD) spectroscopy*, **200**, 470 (1999).

[55] P. Carra, B. Thole, M. Altarelli, and X. Wang, *X-Ray Circular Dichroism and Local Magnetic Fields*, Physical Review Letters **70**, 694 (1993).

[56] A. Tripathi, J. Mohanty, S. H. Dietze, O. G. Shpyrko, E. Shipton, E. E. Fullerton, S. S. Kim, and I. McNulty, *Dichroic coherent diffractive imaging.*, Proceedings of the National Academy of Sciences of the United States of America **108**, 13393 (2011).

[57] C. Donnelly, V. Scagnoli, M. Guizar-Sicairos, M. Holler, F. Wilhelm, F. Guillou, A. Rogalev, C. Detlefs, A. Menzel, J. Raabe, and L. J. Heyderman, *High Resolution Hard X-ray Magnetic Imaging with Dichroic Ptychography*, Physical Review B **064421**, 1 (2016).

[58] G. V. D. Laan, *Applications of soft x-ray magnetic dichroism*, Journal of Physics: Conference Series **430**, 012127 (2013).

[59] O. Kfir, P. Grychtol, E. Turgut, R. Knut, D. Zusin, D. Popmintchev, T. Popmintchev, H. Nembach, J. M. Shaw, A. Fleischer, H. Kapteyn, M. Murnane, and O. Cohen, *Generation of bright circularly-polarized extreme ultraviolet high harmonics for magnetic circular dichroism spectroscopy*, Nature Photonics **9**, 99 (2015).